INTERNATIONAL JOURNAL FOR NUMERICAL AND ANALYTICAL METHODS IN GEOMECHANICS
Int. J. Numer. Anal. Meth. Geomech. (2016)
Published online in Wiley Online Library (wileyonlinelibrary.com). DOI: 10.1002/nag.2657

Particle swarm optimization for numerical bifurcation analysis in computational inelasticity

Zhengshou Lai and Qiushi Chen*,†

Glenn Department of Civil Engineering, Clemson University, Clemson, SC, U.S.A.

SUMMARY

An efficient and robust algorithm to numerically detect material instability or bifurcation is of great importance to the understanding and simulation of material failure in computational and applied mechanics. In this work, an intelligence optimizer, termed the particle swarm optimization, is introduced to the numerical solution of material bifurcation problem consisting of finding the bifurcation time as well as the corresponding bifurcation directions. The detection of material bifurcation is approached as a constrained minimization problem where the determinant of the acoustic tensor is minimized. The performance of the particle swarm optimization method is tested through numerical bifurcation analysis on both small and finite deformation material models in computational inelasticity with increasing complexity. Compared with conventional numerical approaches to detect material bifurcation, the proposed method demonstrates superior performance in terms of both computational efficiency and robustness. Copyright © 2016 John Wiley & Sons, Ltd.

Received 28 June 2016; Revised 18 October 2016; Accepted 20 October 2016

KEY WORDS: material instability; elasto-plasticity; optimization

1. INTRODUCTION

When materials are sufficiently deformed into the inelastic regime, they may exhibit instability or bifurcation in the form of localized zone of intensive deformation. Upon continued loading, such localized deformation or shear band often leads to the complete material failure. In addition to such localized failure mode, a diffuse bifurcation mode may also occur, which has been analyzed in previous studies [1–3]. An efficient and robust method to detect the onset of material bifurcation and the associated bifurcation directions is of great importance to not only the investigation of the bifurcation phenomenon itself but also the development of effective numerical techniques to accommodate such inhomogeneous deformations and to propagate numerical solutions beyond the bifurcation point.

In the context of material bifurcation analysis, existing bifurcation criteria generally fall into four categories [4]: the general bifurcation criterion [5], the limit point criterion [6], the loss of strong ellipticity condition [7], and the classical continuous bifurcation condition [8, 9]. In this work, we adopt the classical continuous bifurcation condition to illustrate the proposed numerical method to detect material instability. The numerical method works for both symmetric and unsymmetric material tangents and can be applied to other bifurcation criteria. The focus will be on the computational efficiency and robustness of the numerical method.

*Correspondence to: Qiushi Chen, Glenn Department of Civil Engineering, Clemson University, Clemson, SC, U.S.A.
†E-mail: qiushi@clemson.edu

1.1. Previous work

The detection of material bifurcation consists of finding the bifurcation time, the associated bifurcation directions and/or the bifurcation mode, for example, localized versus diffusive bifurcation. The bifurcation condition of a material at a given state can be quantified by tracking the determinant of the acoustic tensor constructed from the fourth-order material tangent modulus. Bifurcation occurs if the acoustic tensor loses its positive definiteness, and the associate bifurcation directions are the unit vectors along which the acoustic tensor gives non-positive determinant.

Existing approaches to detect material bifurcation generally fall within analytical closed-form solutions or numerical approaches. The analytical solutions to the bifurcation problem, if available, are typically the most robust and efficient options. Examples of previous work along this line include [8, 10–16]. However, those analytical solutions are only applicable to specific material models and loading conditions upon which they were derived. Analytical solutions to bifurcation problem with more complicated material models and general loading conditions can be extremely difficult to obtain. Such limitations motivate the development of numerical approaches.

Numerical solutions to the material bifurcation problem can be dated back to the work of Ortiz and coworkers [10, 17], in which the constrained minimization problem of bifurcation detection is converted to the equivalent problem of finding eigenvalues of the derivative of the objective function, that is, the determinant of the acoustic tensor. The process consists of two steps. First, an initial sweep in the parametric space of the unit vector is performed to find an estimator of the minimum of the determinant of the acoustic tensor. Second, an iterative algorithm is taken to solve an eigenvalue problem to find the exact solution of the minimization problem. One major assumption of this algorithm is the major symmetry of the material tangent modulus, which is loosened by Sanborn and Pr*é*vost [18] through the modification of the gradient function. An alternative numerical approach used the Newton–Raphson (NR) method to solve the constrained minimization problem of material bifurcation, where the initial guess for the NR iteration is obtained from a sweep through the parametric space of the unit vector [19–22]. Robustness and efficiency of the NR-based methods depend on both the complexity of the objective function and the quality of the initial guess. A relative dense parametric sweep is typically required to ensure convergence of the method. Moreover, the NR-based method requires the derivation of the so-called Jacobian matrix, which could be challenging for complicated material tangent moduli. To avoid the pitfalls of NR-based method, Oliver *et al*. [23] proposed a numerical algorithm based on the iterative solution of a coupled eigenvalue problem in terms of the acoustic tensor. The novel algorithm is rather efficient and robust. However, the solution is only exact for material tangents with both major and minor symmetries and is an approximation otherwise.

In this work, a novel numerical approach to the solution of material bifurcation problem is developed based on an intelligence optimizer, that is, the particle swarm optimization (PSO) [24, 25]. The PSO is an iterative stochastic optimization technique that has been used across a wide range of applications such as image and video analysis, control applications, system identification [26, 27]. Its application in geomechanics community is rare, and a recent effort along this line is the work by Feng *et al*. [28] to develop constitutive model for rock using the PSO algorithm.

In the PSO algorithm, particles are randomly placed within the parametric space of the objective function (e.g., the determinant of the acoustic tensor). The objective function is evaluated at the location of each particle. In subsequent iterations, the movement of an individual particle will be governed by a combination of its own current and best locations (in terms of the optimized objective function value) as well as those of other members. Eventually, collection of all particles, termed the particle swarm, will converge to the optimum of the objective function [27]. The algorithm is very efficient and robust because it does not require computation of any derivative information as in a Newton-type approach. In this work, the proposed PSO-based numerical approach will be tested through applications to the solution of bifurcation problems involving both small and finite deformation material models. Moreover, in constructing the objective function, several common and uncommon parameterizations of the unit vector needed to compute the acoustic tensor are also compared. The proposed numerical approach is compared with existing Newton-based numerical methods to further address its superior performance. Also, the algorithm presented is general and can

DOI: 10.1002/nag

be applied to the numerical bifurcation analysis of both small and finite deformation computational inelasticity problems, regardless of the symmetry of the material tangents.

The remainder of the paper is structured as follows: In Section 2, the general framework for numerical bifurcation analysis is presented, where the classical continuous bifurcation condition is adopted; Section 3 presents the conventional NR-based numerical approaches with several common and uncommon parameterizations; Section 4 details the proposed PSO-based numerical approach as well as its numerical implementation; in Section 5, two numerical examples are presented to evaluate the performance of different numerical approaches followed by conclusions in Section 6.

2. GENERAL FRAMEWORK OF NUMERICAL BIFURCATION ANALYSIS

In this section, the classical continuous bifurcation criterion to identify the onset of material bifurcation and the associated bifurcation directions is briefly presented. The proposed numerical algorithm detailed in Section 4 is general and can be easily applied to other bifurcation criteria, for example, the general bifurcation criterion [5], the limit point criterion [6], or the loss of strong ellipticity condition [7].

2.1. Classical continuous bifurcation criterion

The classical continuous bifurcation criterion states that the loss of material stability and localization will not occur until the acoustic tensor obtains a zero eigenvalue [8, 9]. The necessary condition for the loss of material stability is then

$$\boldsymbol{A} \cdot \boldsymbol{m} = \boldsymbol{0}, \quad \forall\ \boldsymbol{m} \in \mathbb{R}^3. \tag{1}$$

where $\boldsymbol{A}$ is the acoustic or localization tensor, defined as

$$\boldsymbol{A} := \boldsymbol{n} \cdot \mathbb{C} \cdot \boldsymbol{n} \quad \text{or} \quad A_{ik} := n_j C_{ijkl} n_l \tag{2}$$

in which $\mathbb{C}$ is the fourth-order material tangent moduli. It is customary to assume that $\boldsymbol{m}$ and $\boldsymbol{n}$ are unit vectors, that is, $\boldsymbol{m}, \boldsymbol{n} \in \mathcal{S}^2$ where $\mathcal{S}^2 := \{u \in \mathbb{R}^3 \mid \|\boldsymbol{u}\| = 1\}$ is the unit sphere. If condition (1) is satisfied by certain set of $\boldsymbol{n}$ and $\boldsymbol{m}$ at a given loading state, material is said to bifurcate with $\boldsymbol{n}$ and $\boldsymbol{m}$ being the corresponding bifurcation direction and the bifurcation mode, respectively.

To ensure that $\boldsymbol{m}$ in (1) has non-trivial solutions when materials exhibit bifurcation, the determinant of the acoustic tensor $\boldsymbol{A}$ must vanish, that is,

$$\det \boldsymbol{A} = 0, \quad \boldsymbol{n} \in \mathcal{S}^2 \tag{3}$$

which provides a condition for the onset of bifurcation that can be solved by a numerical method.

2.2. Bifurcation detection

The onset of material bifurcation is characterized by the acoustic tensor losing its positive definiteness, that is, when (3) is satisfied. If we assume that the unit vector $\boldsymbol{n}$ is parameterized by a set of variables $\boldsymbol{q}$ and define the objective function $f(\boldsymbol{q})$ as

$$f(\boldsymbol{q}) := \det \boldsymbol{A}(\boldsymbol{q}) \tag{4}$$

Then, the onset of material bifurcation can be equivalently approached by solutions to a constrained minimization problem

$$\min_{\boldsymbol{q}} f(\boldsymbol{q}) = 0, \quad \boldsymbol{n}(\boldsymbol{q}) \in \mathcal{S}^2 \tag{5}$$

When the condition (5) is satisfied, the material bifurcates and its associated bifurcation direction can be obtained in terms of the unit vector $\boldsymbol{n}$.

DOI: 10.1002/nag

Remark 1
In the actual numerical simulation, due to the finite size of a loading step, condition (5) may not be satisfied exactly. Instead, an adaptive time step algorithm [22] will be implemented in this work. Consider the original time increment from time t_n to t_{n+1}, where the minimum of the objective function $\mu_n := \min_q f(\boldsymbol{q}) > 0$ and $\mu_{n+1} < 0$. This means that between time t_n and t_{n+1}, condition (5) is satisfied and therefore material bifurcates. In the adaptive time step algorithm, the time step size will be repeatedly cut until the new minimum of the objective function $\mu_{n,k}$ is within a small set tolerance around zero after the kth iteration.

3. NEWTON–RAPHSON-BASED NUMERICAL APPROACHES AND PARAMETERIZATIONS

If the determinant function $f(\boldsymbol{q})$ is differentiable, the minimization problem can be rewritten equivalently as

$$\frac{\partial f}{\partial \boldsymbol{q}}(\boldsymbol{q}) = 0 \tag{6}$$

Existing numerical bifurcation analysis [10, 17, 20–22] relies on a NR-type iterative method to solve the minimization problem defined in (6). In a NR-based approach, the numerical detection of the bifurcation condition for each time increment consists of the following two steps [22]:

- Sampling step: An initial sampling or sweeping is performed over the parametric space of $\boldsymbol{q}$ for the normal vector $\boldsymbol{n} \in S^2$. At each of the sampling point, the determinant function (4) is evaluated. This leads to a rough estimation of the minimum of the determinant function (5) and the associated bifurcation directions.
- Optimization step: The coarse estimate is then used in the optimization step to initiate an iterative procedure to find a more accurate estimate of the onset of bifurcation and its associated directions by solving the minimization problem (6).

Efficient and robust solution of the minimization problem (5) or (6) requires a careful choice of the parameterization for the unit vector $\boldsymbol{n}(\boldsymbol{q}) \in \mathcal{S}^2$. As shown in a recent work [22], this choice of parameterization has a significant effect on the complexity of the determinant function $f(\boldsymbol{q})$. In this work, a total of four different parameterizations will be considered in the NR-based numerical approaches and compared with the newly proposed method to be discussed in Section 4. Figure 1 shows the four parameterizations considered in this work, which are briefly discussed herein. For more details, the reader is referred to [22]. It should be pointed out that, due to symmetry of the bifurcation condition, only half of the spherical parametric domain or half of the cubic parametric domain needs to be searched as given by the ranges of the parameters.

- Spherical parameterization: This parameterization is the most commonly used [20, 21], where elements of the unit vector $\boldsymbol{n}(\boldsymbol{q})$ of the unit sphere $\mathcal{S}^2$ are simply parameterized by their spherical coordinates with the polar angle $\varphi \in [0, \pi]$, the azimuthal angle $\theta \in [0, \pi]$ and the radial distance $r = \|\boldsymbol{n}\| = 1$, written as

$$\boldsymbol{n}(\boldsymbol{q}) = \boldsymbol{n}(\varphi, \theta) := \left\{ \begin{array}{l} \sin\varphi\cos\theta \\ \sin\varphi\sin\theta \\ \cos\varphi \end{array} \right\} \tag{7}$$

- Projective parameterization: In the projective parameterization, the norm of the position vector of a point P with respect to the center of the unit sphere $\mathcal{S}^2$ is constrained in length to obtain a unit vector $\boldsymbol{n}$. A Lagrange multiplier can be introduced to constrain any norm vector into unit length, as used by Ortiz *et al*. [17] and Leroy *et al*. [10] and written as

DOI: 10.1002/nag

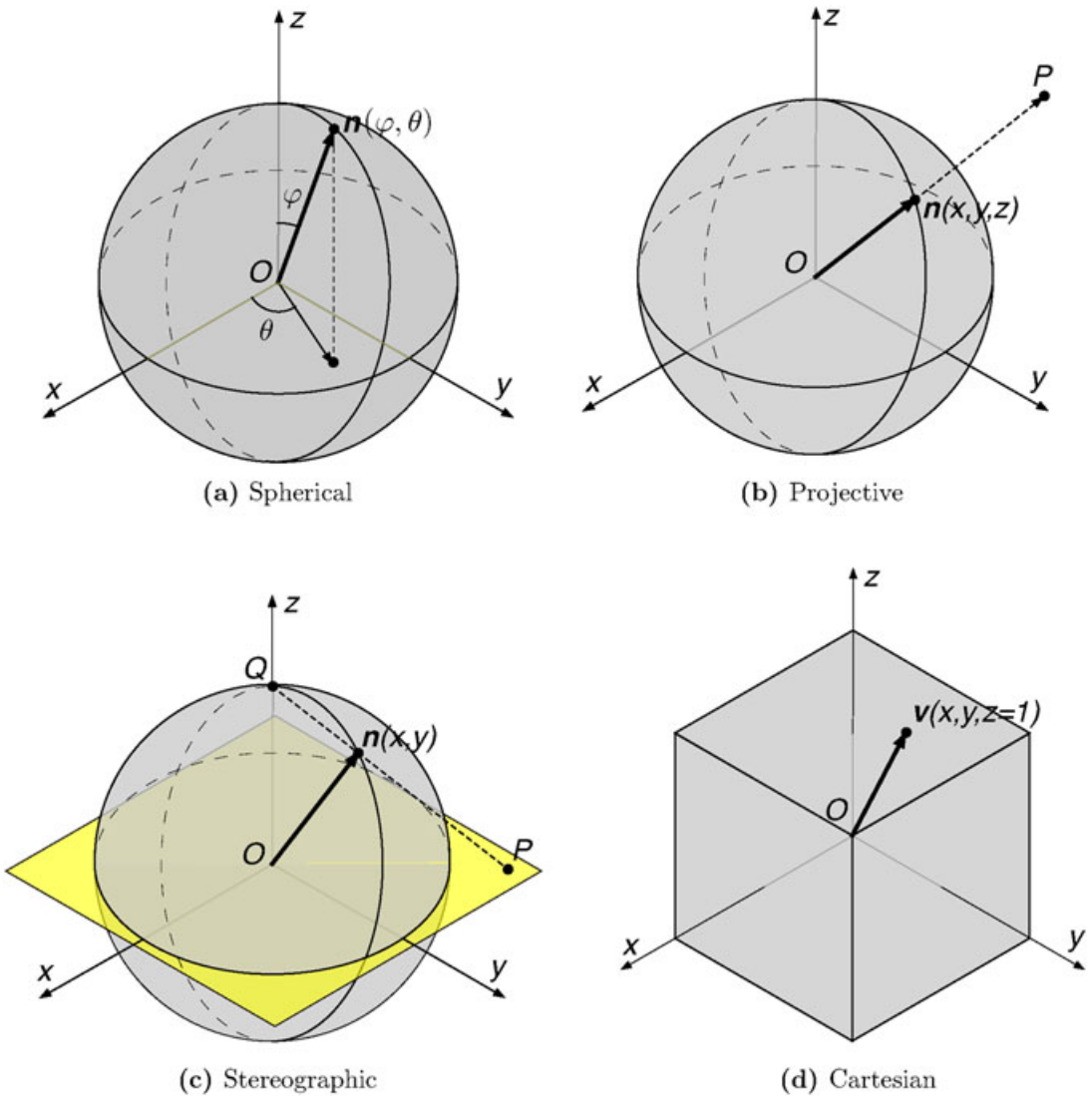

Figure 1. The four parameterizations used in Newton–Raphson-based numerical approaches to detect material bifurcation (adopted from [22]).

$$\boldsymbol{n}(\boldsymbol{q}) = \boldsymbol{n}(x, y, z) := \left\{ \begin{array}{c} x \\ y \\ z \end{array} \right\}, \quad \text{subjected to } x^2 + y^2 + z^2 = 1. \tag{8}$$

where the parameters $x \in [-1, 1]$, $y \in [-1, 1]$ and $z \in [0, 1]$.

- Stereographic parameterization: This option parameterizes the unit sphere $\mathcal{S}^2$ with the aid of an equatorial plane. The normal vector $\boldsymbol{n}$ in terms of the canonical basis can be written as

$$\boldsymbol{n}(\boldsymbol{q}) = \boldsymbol{n}(x, y) := \left\{ \begin{array}{c} \frac{2x}{x^2+y^2+1} \\ \frac{2y}{x^2+y^2+1} \\ \frac{x^2+y^2-1}{x^2+y^2+1} \end{array} \right\} \tag{9}$$

where the parameters $x \in [-1, 1]$ and $y \in [-1, 1]$.

- Cartesian parameterization: The Cartesian parameterization is recently proposed by Mota *et al*. [22], where the restriction that the normal vector be of unit length is relaxed. Denote the

DOI: 10.1002/nag

normal vector as $\boldsymbol{v}$, the Cartesian parameterization of the vector $\boldsymbol{v}$ is given as

$$\boldsymbol{v}(\boldsymbol{q}) = \boldsymbol{v}(x, y, z) := \begin{cases} [x, y, 1]^T, & \text{if } x \in [-1, 1] \text{ and } y \in [-1, 1); \\ [1, y, z]^T, & \text{if } y \in [-1, 1] \text{ and } z \in [-1, 1); \\ [x, 1, z]^T, & \text{if } z \in [-1, 1] \text{ and } x \in [-1, 1); \\ [1, 1, 1]^T, & \text{otherwise.} \end{cases} \tag{10}$$

This parameterization confines the normal vector to the @@cube of side length two centered at the origin of the unit sphere $\mathcal{S}^2$. It has been shown in [22] that using the normal vector $\boldsymbol{v}$ in place of $\boldsymbol{n}$ in (2) leads to the same bifurcation condition.

The four parameterizations shown in Figure 1 are used with the NR-based numerical approaches to detect material bifurcation. Regardless of the parameterizations, the NR-based numerical approaches typically adopt the two-step solution scheme described at the beginning of this section, where the quality of the initial sampling greatly affects the efficiency and robustness of the numerical approaches. This point will be further illustrated in the numerical example section. All NR-based approaches solve the constrained minimization problem (6), which requires that the determinant function $f(\boldsymbol{q})$ to be twice differentiable. In the next section, a novel method is introduced to the numerical solution of material bifurcation problem (5). This method is based on a stochastic algorithm, termed the PSO, that does not have such constrain on the determinant function and the initial sweep stage is no longer needed.

4. PARTICLE SWARM OPTIMIZATION FOR BIFURCATION DETECTION

Particle swarm optimization is a stochastic algorithm that is based on social-psychological principles [29]. It is originally proposed by Eberhart and Kennedy [24] and Eberhart *et al*. [25]. The development of the particle swarm method is inspired by the flight behavior of flocks of birds, that is, the birds are more likely to fly toward individual and group's best position, where there is more food or less flight resistance. There are a variety of modifications and implementations of the particle swarm method dealing with challenges such as local versus global minimum and multiple minima [26, 30, 31].

In this section, we will develop a PSO-based numerical approach to solve the constrained optimization problem (5) for the numerical detection of material bifurcation.

4.1. The particle swarm optimization algorithm

In the PSO algorithm, a group of particles, referred to as a particle swarm, are randomly placed or initialized in the parametric space, within which the objective function is to be evaluated. The movement of individual particle within the swarm is governed by a combination of its own current and past best locations (in terms of the objective function value) as well as those of other members.

Consider the objective function $f(\boldsymbol{q})$ in (5) with its dependent variable $\boldsymbol{q}$, which is a vector of real number of D dimensions, that is, $\boldsymbol{q} \in \mathbb{R}^D$. The objective here is to find $\boldsymbol{q}^*$ that gives the extreme (minimum) values of the objective function $f(\boldsymbol{q}^*)$. To this end, a group of particles represented by vectors $\boldsymbol{q}_i$ are randomly placed in the search space of the parameter sets, with $i = 1, 2, \ldots, N$ indicating the particle index and usually $10 < N < 100$. Denote $\boldsymbol{q}_{ib}$ as the best position ever detected by the ith particle, and $\boldsymbol{q}_{gb}$ as the best position ever detected by the group, with the corresponding objective function values $f_{ib} = f(\boldsymbol{q}_{ib})$ and $f_{gb} = f(\boldsymbol{q}_{gb})$, respectively. Then, the movement of each particle characterized its velocity $\boldsymbol{v}_i$ at $(k+1)$th iteration (also referred to as *time step* in the PSO literature) is given as [28, 31, 32]

$$\begin{aligned} \boldsymbol{v}_i^{k+1} &= w\boldsymbol{v}_i^k + c_1\xi\boldsymbol{v}_{ib} + c_2\eta\boldsymbol{v}_{gb} \\ &= w\boldsymbol{v}_i^k + c_1\xi(\boldsymbol{q}_{ib} - \boldsymbol{q}_i^k) + c_2\eta(\boldsymbol{q}_{gb} - \boldsymbol{q}_i^k) \end{aligned} \tag{11}$$

where i is the target particle's index; w is a parameter called the inertia weight; c_1 and c_2 are positive constants, referred to as the cognitive and social parameters, respectively; ξ and η are two random numbers uniformly distributed in [0, 1], which are randomly generated for each particle at

DOI: 10.1002/nag

each iteration; $\boldsymbol{v}_{ib}$ and $\boldsymbol{v}_{gb}$ are the components of particle velocity influenced by the individual and group's best location $\boldsymbol{q}_{ib}$ and $\boldsymbol{q}_{gb}$, respectively.

Once the velocity is determined, the position of the ith particle at the $(k+1)$th iteration is updated as

$$\boldsymbol{q}_i^{k+1} = \boldsymbol{q}_i^k + \zeta \boldsymbol{v}_i^{k+1} \tag{12}$$

where ζ is called the constriction factor and is introduced to limit the impact of previous histories of velocity on the current particle position [31, 33].

For each iteration, the best locations $\boldsymbol{q}_{ib}$ and $\boldsymbol{q}_{gb}$ will be updated based on values of the objective function $f(\boldsymbol{q}_i^k)$ of individual particles as well as other members in the swarm. The particle swarm as a whole will evolve toward an optimum.

The movements of the ith particle between three consecutive iterations, $k-1$, k, and $k+1$, are illustrated in Figure 2. As shown in the figure, the velocity of this particle at the $(k+1)$th iteration consists of three parts: $\boldsymbol{v}_{ib}$, $\boldsymbol{v}_{gb}$, and $\boldsymbol{v}_i^k$ as indicated in the figure. By adjusting the appropriate weights on different velocity components, the particle will eventually evolve toward the best (group) optimum.

The update of particle positions will be repeated until certain convergence criterion is met. Currently, there is no universal criterion for the convergence of the PSO method. In this work, we use a simple form by checking the standard deviation σ_ϵ of individual's best location with respect to the group's best location, expressed as

$$\sigma_\epsilon = \sqrt{\frac{1}{N}\sum_{i=1}^{N}\left(f_{ib}^k - f_{gb}\right)^2} \tag{13}$$

When the aforementioned standard deviation is within a set tolerance ϵ, the algorithm is said to converge.

4.2. *Numerical implementation*

In this work, the PSO-based numerical solution to the bifurcation problem (5) is implemented into Sandia National Laboratories' open-source finite element code Albany [34–36]. The Albany code is designed for the rapid development of finite element analysis capabilities enabled through the concept of *agile components*; generic building blocks of capabilities are readily assembled to meet the

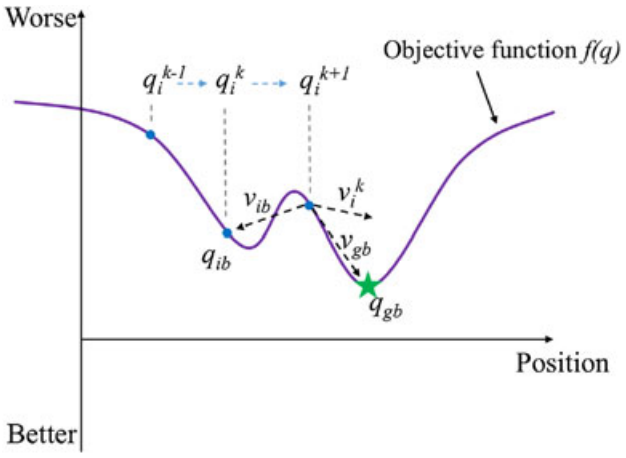

Figure 2. The PSO method: sketch of the ith particle evolution during three consecutive iterations $k-1$, k, and $k+1$. The lower indices ib and gb refer to the individual and group's best position, respectively. The star indicates location of the global minimum.

DOI: 10.1002/nag

requirements of the ultimate analysis application. Albany has been successfully used to solve problems in nuclear applications [37, 38], geomechanics problems [39, 40], uncertainty quantification [41, 42]. Albany is now open source and can be downloaded at the website given in the bibliography [36].

The flowchart of the PSO-based algorithm is shown in Figure 3. The fourth-order material tangent moduli $\mathbb{C}$ is provided by the constitutive model evaluator in the Albany analysis code to construct the constrained minimization problem (5). The objective function is the determinant of the acoustic tensor, that is, $f(\boldsymbol{q}) = \det \boldsymbol{A}(\boldsymbol{q})$. The solution of the PSO-based algorithm provides the optimum (minimum) value of the objective function f_{gb} as well as the associated parameter value $\boldsymbol{q}_{gb}$. f_{gb} will be used to check if material bifurcation condition (5) is satisfied and the associated bifurcation directions can be calculated using the parameter $\boldsymbol{q}_{gb}$ and expressed in terms of the unit vector $\boldsymbol{n}(\boldsymbol{q}_{gb})$. The maximum number of iteration, denoted as $k_{\max}$ in Figure 3, is introduced as a safeguard

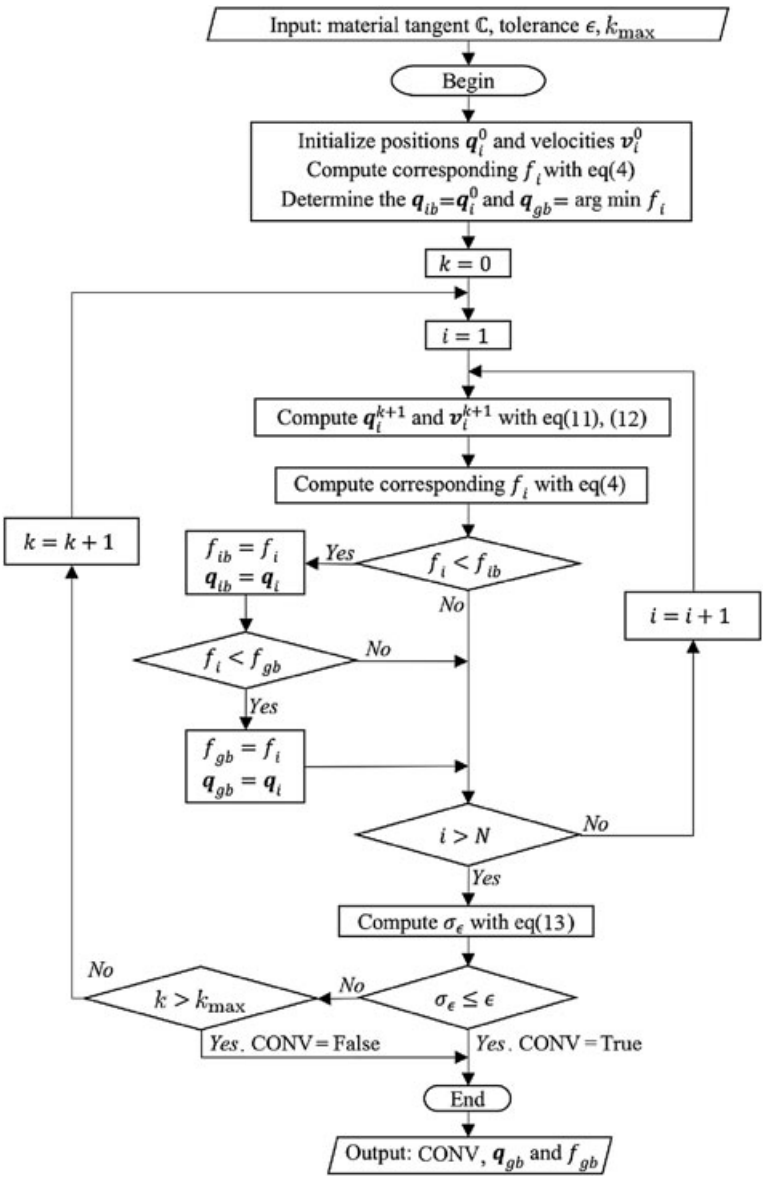

Figure 3. Flowchart of the PSO-based numerical algorithm to detect material bifurcation. $k_{\max}$ is the maximum allowed number of iterations, CONV is a convergence flag to indicate the convergence condition, and ϵ is the set tolerance for the PSO convergence criterion (13).

DOI: 10.1002/nag

to avoid an endless loop when the algorithm encounters a convergence issue. If convergence cannot be achieved after $k_{\max}$ iterations, the swam population N should be increased.

The PSO-based algorithm will be used to check the bifurcation condition at every integration point within every element for every time step during a finite element simulation. Hence, its performance in terms of computational efficiency and robustness is of particular concern. This will be illustrated through numerical examples in Section 5. Here, it is worth noting that the proposed PSO-based algorithm is particularly suitable for parallel implementation and execution [43]. The evolution of each particle only depends on its own history as well as the group's best. As a result, each particle can be evaluated in a separate computing unit, which will further improve the computational efficiency and is of great advantage to be used within large-scale finite element simulations.

Remark 2
The proposed PSO-based algorithm also requires the parameterization of the normal vector $\boldsymbol{n}$ used in constructing the determinant function (2). Here, we choose to compare results of the stereographic parameterization (9) because the focus is on PSO method itself rather than the parameterizations. Also, the stereographic parameterization only involves simple arithmetic operations and is slightly more efficient to evaluate than the spherical parameterization.

Remark 3
One of the major advantages of the proposed PSO-based method, in terms of implementation, is that the PSO-based approach does not need to evaluate the gradient of the determinant function nor the assemble of Jacobian matrix required by the NR-based approaches. For complex material models, these derivative calculations can be quite complex and error-prone.

4.3. Particle swarm optimization parameters and group diversity

4.3.1. Particle swarm optimization parameters. The performance in terms of computational efficiency and robustness of the PSO-based algorithm to detect material bifurcation relies on the careful choice of algorithm parameters used in updating the particle velocity (11) and location (12). The algorithm parameters include the inertia weight w, the cognitive and social parameters c_1 and c_2, the constriction factor ζ, and the group or swarm size N.

The inertia weight w in (11) dictates to what extent an individual particle will preserve its previous history of velocities, and its typical range is $0 < w < 1$. This parameter is critical for the convergence behavior and resolves the tradeoff between the global and the local exploration ability of the swarm [31]. The exact value of w is problem dependent, but previous experience suggests an initial value of w around 1 and a gradual decline toward 0 to achieve superior performance [31, 44, 45].

The cognitive and social parameters c_1 and c_2 in (11) control the tendency of a particle moving toward the individual or the group's best positions. Their influence on the algorithm convergence is less critical compared with the inertia weight w. However, the choice of parameter values for c_1 and c_2 should satisfy the constraint $c_1 + c_2 < 4(1 + w)$ to avoid convergence issue [32]. Experiments from Trelea [46] indicate that large values of c_1 and c_2 may cause harmonic oscillations and zigzagging of particle movements. Common practice suggests a general set $c_1 = c_2 = 1.494$ with $w = 0.729$, which is verified to have great convergence behavior for a variety of test functions. The study of Parsopoulos and Vrahatis [44] also proposed a default sets of $c_1 = c_2 = 0.5$. Alternative combination of values, depending on the problem, may produce superior performance.

The constriction factor ζ in (12) is introduced to limit the impact of previous histories of velocity on current particle position and effectively scale the velocity to within a set limited bound [31, 33]. Clerc and Kennedy [33] introduced the following formula that can be used to obtain the constriction factor

$$\zeta = \frac{2k}{\|2 - \phi - \sqrt{\phi^2 - 4\phi}\|} \tag{14}$$

for $\phi > 4$, where $\phi = c_1 + c_2$ and $k \in [0,\ 1]$. For $\phi \leq 4$, $\zeta = k$ [33].

DOI: 10.1002/nag

Alternatively, a maximum allowed velocity $\boldsymbol{v}_{max}$ can be used to bound the particle velocity. This bound on maximum particle velocity will avoid severe mutation of particles.

The group or swarm size N affects the speed of convergence as well as the robustness of the algorithm. The optima group size is problem dependent. A typical range of $10 < N < 100$ is suggested by Kennedy [29] and has been shown effective for most problems.

In the numerical examples section, influence of algorithm parameters on the performance of the PSO-based numerical method will be investigated. Recommendations on the optimal combination will be given. The recommended set of algorithm parameters will be used for all numerical models and loading conditions.

4.3.2. Group diversity. Particle swarm optimization is a stochastic algorithm in which individual particle is randomly placed in the search space of the objective function to find optimized function values. Herein, group diversity refers to the diverse or randomized locations and movements of individual particles. Such diverse or random feature renders the algorithm particularly effective and robust in finding optimized solutions to very complex objective functions.

The group diversity or randomness of the PSO-based algorithm comes from the initial random placement of particles in the search domain, and the two random numbers ξ and η in (11). The presence of these two random numbers improves the exploration and prevents premature convergence to non-optimal positions [46]. In a diverse group, particles are scattered and move to all kinds of locations, such as multiple local or global minima, which provide better performance in terms of both computational efficiency and robustness [47, 48]. The superior performance of the proposed PSO-based numerical algorithm to detect material bifurcation will be illustrated in the numerical example section.

5. NUMERICAL EXAMPLES

In this section, the performance of the proposed PSO-based algorithm will be evaluated using two material models subjected to various loading conditions. Material models considered include a small deformation two-invariant Drucker–Prager (DP) plasticity model and a finite deformation anisotropic damage model.

The purpose of the numerical examples is to investigate the performance of the proposed algorithm in terms of computational efficiency (i.e., computation time) and robustness (i.e., its ability to correctly detect material bifurcation). First, a preliminary investigation on the influence of the PSO parameters will be presented using the DP model. Results from this study will be used to guide parameter selection. Then, all the subsequent numerical examples use the same set of PSO parameters.

For comparison purposes, the classical NR-based numerical methods will be implemented with four parameterizations described in Section 3 termed as NR-spherical, NR-projective, NR-stereographic and NR-Cartesian, in the following examples.

Remark 4
All the simulations presented are conducted on a PC workstation with Intel Xeon(R) CPU E3-1241 v3 @ 3.5GHz × 8 processor. The code base is Sandia National Laboratories' Albany code [34–36].

5.1. Small deformation Drucker–Prager plasticity model

The first numerical example is the bifurcation analysis of a small deformation two-invariant DP plasticity model [49] subjected to plane strain compression. The DP model has been widely used to simulate the frictional-dilative behavior of granular materials. The analytical solutions of the bifurcation condition for the DP model are quite tractable [8, 11, 16], which will be used to verify solutions of the numerical algorithms. Also, the selection of PSO parameters will be investigated and results will be used to guide other numerical examples.

5.1.1. Model formulation. The yield function, denoted as F, and the plastic potential function, denoted as G, of the DP model can be written in terms of two stress invariants as

DOI: 10.1002/nag

$$F = q + \alpha p - c_f \tag{15}$$

$$G = q + \beta p - c_q \tag{16}$$

where p and q are stress invariants defined as $p = \frac{1}{3}\boldsymbol{\sigma} : \boldsymbol{\delta}$ and $q = \frac{3}{2}(\boldsymbol{s} : \boldsymbol{s})^{1/2}$; $\boldsymbol{s}$ is the deviatoric stress tensor, $\boldsymbol{s} = \boldsymbol{\sigma} - p\boldsymbol{\delta}$, with $\boldsymbol{\sigma}$ being the Cauchy stress tensor and $\boldsymbol{\delta}$ being the Kronecker delta; α, β are the internal variables correlated with the angle of friction and dilatancy of the material; c_f is a cohesion parameter and typically $c_f = 0$ for dry granular materials; c_q is a cohesion-like parameter used in the plastic potential function.

For the hardening law governing the evolution of the two internal variables α and β, we adopt a simple exponential type flow rule as [50]

$$\alpha = a_0 + a_1\gamma \exp(a_2 p - a_3\gamma) \tag{17}$$

$$\beta = \alpha - b_0 \tag{18}$$

where a_0, a_1, a_2, a_3, and b_0 are positive material constants; γ is the cumulative plastic multiplier.

Using the consistency condition and the additive decomposition of the small strain tensor into an elastic and a plastic component, the elasto-plastic fourth-order material tangent $\mathbb{C}^{\mathrm{ep}}$ can be derived as

$$\mathbb{C}^{\mathrm{ep}} = \mathbb{C}^{\mathrm{e}} - \frac{1}{\chi}\mathbb{C}^{\mathrm{e}} : \boldsymbol{g} \otimes \boldsymbol{f} : \mathbb{C}^{\mathrm{e}} \tag{19}$$

where $\mathbb{C}^{\mathrm{e}}$ is the fourth-order elasticity tensor; $\boldsymbol{f} = \frac{\partial F}{\partial \boldsymbol{\sigma}}$ and $\boldsymbol{g} = \frac{\partial G}{\partial \boldsymbol{\sigma}}$ are the stress gradients of the yield function and plastic potential function, respectively. The variable χ is expressed as

$$\chi = \boldsymbol{f} : \mathbb{C}^{\mathrm{e}} : \boldsymbol{g} + \mathcal{H} \tag{20}$$

with the generalized hardening modulus $\mathcal{H}$ given as

$$\mathcal{H} = -\frac{\partial F}{\partial \alpha}\frac{\partial \alpha}{\partial \gamma} \tag{21}$$

5.1.2. Plane strain compression. In this section, a plane strain compression test is simulated as shown in Figure 4, where $\boldsymbol{n}$ is the outward norm of the bifurcation band. The lateral confining pressure for the plane strain test is set to 50 kPa. Constant material parameters are taken from [50]: the elasticity constants $E = 25,000$ kPa and $\nu = 0.3$; parameters for hardening law $a_0 = 0.7$, $a_1 = 50$, $a_2 = 0.0005$ 1/kPa, $a_3 = 50$, $b_0 = 0.7$, and $c_f = c_q = 0$. **F4**

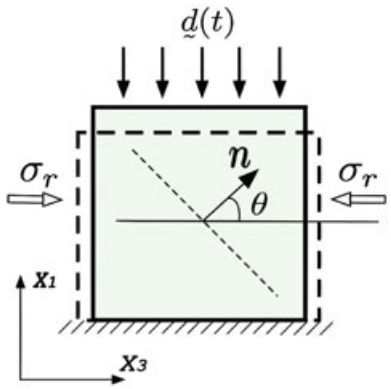

Figure 4. Schematic of the plane strain compression test with the original (solid boundary) and deformed (dashed boundary) element. $\boldsymbol{n}$ is the outward norm of the bifurcation plane and θ is the angle between norm $\boldsymbol{n}$ and the X_3 axis. $d(t)$ is the prescribed axial displacement and σ_r is the confining stress.

DOI: 10.1002/nag

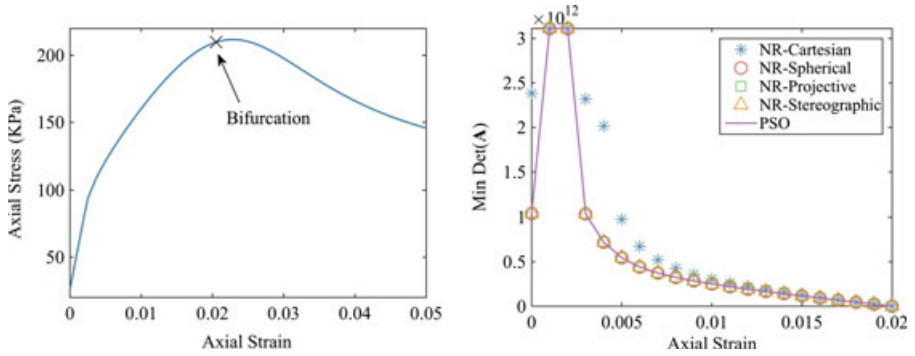

Figure 5. Plane strain compression test on the Drucker–Prager plasticity model: (a) stress–strain behavior; and (b) degradation of min(det $\boldsymbol{A}$).

Figure 5(a) shows the axial stress–strain behavior in the plane strain compression test along with the point when material bifurcation is detected. Softening response is reached shortly following the point where the bifurcation condition is first met. Figure 5(b) shows the degradation of the minimum of the objective function (det $\boldsymbol{A}$) for all five numerical approaches tested. In the simulation, an adaptive time described in Section 2.2 is used so that the precise time of bifurcation can be detected. When the minimum of the objective function is zero, material bifurcates and the associated bifurcation directions in terms of the unit vectors $\boldsymbol{n}$ are calculated from the optimum parameter set $\boldsymbol{q}^*$. For this plane strain compression example, all five types of numerical approaches detect the material bifurcation at the same time, that is, when the axial strain $\epsilon_{11} = 0.0201$, and the corresponding bifurcation direction is given in terms of the unit vector $\boldsymbol{n} = (0.564945, 0, 0.825129)$. It should be noted that, in this example, there are two conjugate solutions of the bifurcation direction, that is, multiple global minima exist. The numerical algorithms including the proposed PSO detect and return only one of the minima. The initial particle position in the PSO algorithm or the initial guess of a NR-based approach affects which one of these minima is detected and returned. In the case of an anisotropic material model as will be shown in the second numerical example, the proposed PSO algorithm is able to detect the true global minima. A recent study [51] includes an interesting and more detailed discussion on conjugate and dominant localization bands for isotropic and anisotropic material models.

The analytical solution to the bifurcation problem of the DP model has been derived in a number of previous work [8, 11, 16]. Denote the bifurcation plane as the $X_1 - X_3$ plane, the corresponding bifurcation direction can be defined in terms of the angle θ between the normal vector $\boldsymbol{n}$ and the X_3 axis shown in Figure 4. The critical hardening modulus $\mathcal{H}^*$ and the corresponding bifurcation angle θ at bifurcation could be derived as [11]

$$\mathcal{H}^* = \frac{\mu(1+\nu)}{18(1-\nu)}[2(\alpha-\beta)^2 - (1-\nu)(\frac{9s_3}{q} + \alpha + \beta)^2] \tag{22}$$

$$\tan^2\theta = -\frac{9(s_1 + \nu s_2) + (1+\nu)q(\alpha+\beta))}{9(s_3 + \nu s_2) + (1+\nu)q(\alpha+\beta))} \tag{23}$$

where s_1, s_2, and s_3 are the principal deviatoric stresses; ν is the Poisson's ratio; μ is the shear modulus; α and β are the two internal variables in the DP model.

Figure 6 plots the hardening modulus (numerical vs. analytical) as a function of applied axial strain. For the numerical solution, the hardening modulus is computed at each axial strain level. The analytical solution shown in the figure is the critical hardening modulus required for material to bifurcation. At material bifurcation, the hardening modulus predicted by the PSO numerical method is $\mathcal{H}^* = 270.4$ kPa, which matches exactly the analytical critical modulus using (22).

DOI: 10.1002/nag

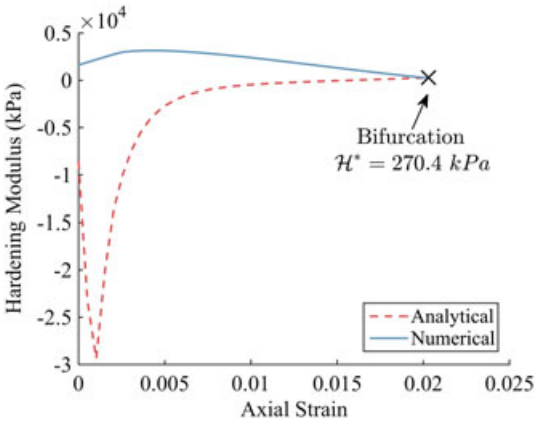

Figure 6. Evaluation of hardening modulus as a function of the applied axial strain. At material bifurcation, numerical hardening modulus matches the critical hardening modulus given by analytical solution.

Table I. Computational cost of different PSO parameter combinations in the plane strain compression test on the Drucker–Prager model at the onset of bifurcation.

	w (run time in μs)					
c_1, c_2	0.5	0.6	0.7	0.8	0.9	1.0
0.1	–	–	–	1135	399	–
0.3	–	79	106	119	400	–
0.5	62	82	111	185	410	–
0.7	68	86	130	188	530	–
0.9	73	87	122	201	597	–
1.5	68	112	172	390	1107	–
2.0	137	193	314	1159	–	–

The run time for each parameter combination is given in μs. The dash '–' indicates that the parameter combination fails to detect bifurcation.

The bifurcation direction from numerical solution is $\boldsymbol{n} = (0.564945, 0, 0.825129)$, which matches exactly to the bifurcation angle $\pm 34.40°$ calculated using the analytical solution (23).

5.1.3. Particle swarm optimization parametric study. To guide the selection of the PSO algorithm parameters and to understand their influence on the efficiency and robustness of the numerical method, we perform a parametric study on three key PSO parameters in (11), that is, the inertia weight w, the cognitive and social parameters c_1 and c_2. The material tangent modulus at the onset of material bifurcation is used as the input to test the performance of different parameter combinations. The results in terms of computation time are summarized in Table I.

As seen from Table I, the PSO method is rather robust for majority of the parameter combinations except when $w = 1$ or when $c_1 = c_2 = 0.1$. The parameter range of $w \in [0.6,\ 0.8]$ and $c_1, c_2 \in [0.3,\ 0.9]$ is recommended. In all subsequent examples, we will pick one parameter combination from this recommended range, that is, $w = 0.7$, and $c_1 = c_2 = 0.5$, for the PSO method. We will illustrate that the PSO method is very robust with respect to this parameter combination. This combination is also consistent with recommendations by Parsopoulos and Vrahatis [44] based on testing of a variety of different objective functions. The group size N and the constriction factor ζ have less influence on the convergence behavior and $N = 10$ and $\zeta = 1.0$ will be set for all examples.

DOI: 10.1002/nag

5.1.4. Efficiency and robustness analysis. While Figure 5 shows that all numerical approaches correctly detect material bifurcation, it provides little information on their computational efficiency and robustness, which are the focus of this work. To quantify the computational cost of different approaches, the time spent on bifurcation detection at a particular loading increment, for example, at the increment leading to bifurcation, is recorded. Results of computational cost are plotted in Figure 7. It should be pointed out that, for NR-based approaches, the efficiency and robustness depend greatly on the density of the grid used for the initial sampling (refer Section 3 for the two-step procedure for NR-based approaches). The computation time shown in Figure 7 for NR-based approaches is from successful runs with the most efficient grid density. Because NR-based approaches are very sensitive to the initial guess, in practice, a very dense grid is typically required for NR-based approaches, which means that the NR-based approaches could be far less efficient than the results shown in Figure 7. This point will be illustrated in the subsequent robustness analysis.

Figure 8 shows the landscapes of the determinant function ($\det \boldsymbol{A}$) at the onset of material bifurcation using Cartesian, spherical, and stereographic parameterizations, the result of projective parameterization is not visualizable in the landscape because it is formulated with three parameters. Multiple minimum as well as bumps are observed in these complex landscapes, which can result in significant difficulties for NR-based approaches.

For the NR-based approaches, the sweep over a prescribed grid provides the initial guess to the subsequent Newton iterative scheme. The quality of this initial guess would greatly affect the computational efficiency and robustness of NR-based approaches. To elaborate the influence of the initial guess, a situation eliminating sweep stage is investigated. Herein, a random point within the corresponding parametric space is provided as the initial guess for the NR-based approach. If a particular NR approach is able to correctly detect the onset of bifurcation and its associated directions, this

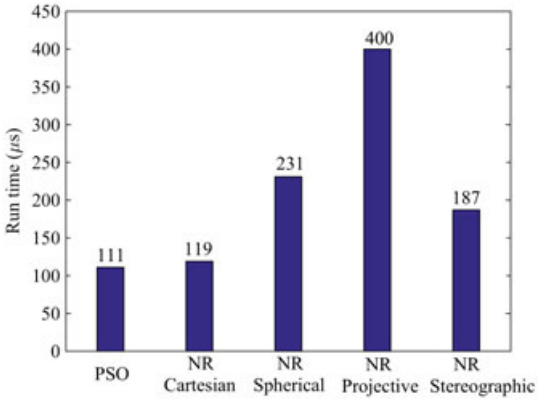

Figure 7. Plane strain compression test on the Drucker–Prager model: comparison of run time (in μs) for different numerical methods to detect material bifurcation.

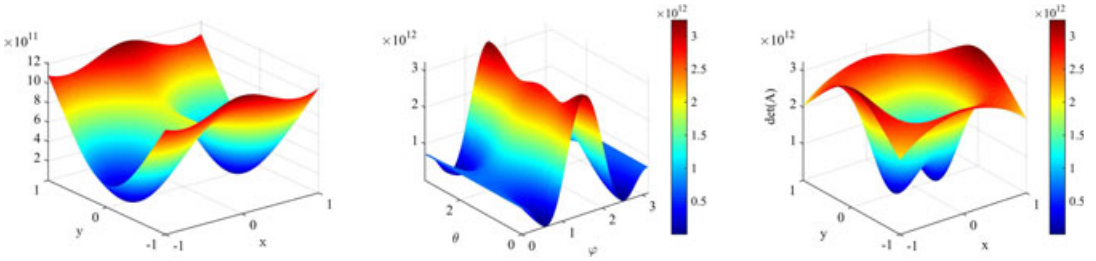

(a) Cartesian (b) Spherical (c) Stereographic

Figure 8. Landscape of the determinant function $\det \boldsymbol{A}$ at the onset of material bifurcation during the plane strain compression test on the Drucker–Prager model using different parameterizations.

DOI: 10.1002/nag

NR approach is said to succeed for this one set of randomly generated parameters. This process is repeated 1000 times for each NR-based approach.

Figure 9 shows the results from 1000 random runs for three types of NR-based approaches. It can be seen that the success rate varies greatly among different types of parameterizations. One interesting phenomenon is that some crosses are fairly close to the correct solution (red star), which means that even if those initial guesses are very close to the correct solution, the numerical approach fails to correctly detect material bifurcation. To assure success, a much denser grid needs to be constructed for the initial sweep, which would in return degrade the computational efficiency.

For the proposed PSO method, once the PSO parameters are selected, its robustness is mainly affected by the randomness of initial particle positions and the two uniformly distributed random numbers ξ and η in (11) for updating particle velocities. Again, using material tangent at the onset of bifurcation, 1000 repeated runs of bifurcation check using the PSO method are performed.

To make a fair comparison in terms of computation time and success rate, a situation is also investigated where an initial sweep with N randomly placed points within the parametric space are used in the NR-based approach. A total of 1000 random runs are performed. Results of computation time and success rate are summarized in Table II. It can be seen from the table that the PSO method takes more iteration counts to solve the optimization problem. However, because the PSO method does not need to compute the Jacobian matrix of the objective function as required in a NR iterative solve, the averaged run time for the PSO method is much less compared with the NR-based approaches. Among various NR-based approaches, the NR-Cartesian is the most efficient and the NR-projective is the most robust one. The most notable feature of the PSO method is its 100% success rate when it comes to correctly detect material bifurcation and the associated directions. In contrast, the NR-based approaches are greatly affected by the quality of its initial guesses and a poor initial guess will result in the failure of the method. A recent study [22] has also investigated the robustness of NR-based approaches as a function of the number of initial points, where it is found that the NR-Cartesian approach is the most robust among all NR-based approaches, which is consistent with the results shown in Table II.

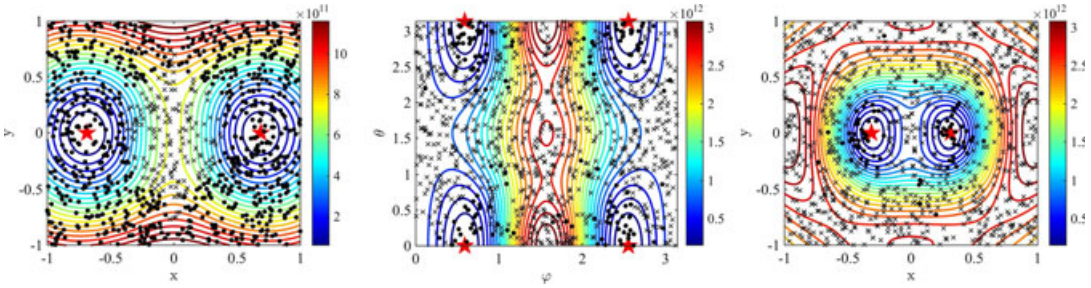

(a) Cartesian (b) Spherical (c) Stereographic

Figure 9. Robustness study for NR-based approach with a single random initial guess for minimizing the determinant function at bifurcation. A solid circle (•) indicates that the initial point leads to a successful detection of bifurcation and its directions. A cross (×) indicates failure. The red star indicates the bifurcation solution. A total of 1000 random trials are performed for each parameterization.

Table II. Success rate and averaged computation time of different numerical approaches with random initial points (for NR-based approaches) or random initial particle positions (for the PSO algorithm).

	PSO	NR-Cartesian	NR-Spherical	NR-Projective	NR-Stereographic
Success rate (%)	100	83.4	67.8	63.7	52.6
Iteration count	89.7	6.25	4.06	9.62	4.27
Run time (μs)	126	235	233	539	226

The averaged iteration count and run time are computed using the successful runs only.

DOI: 10.1002/nag

In the PSO method, the randomly placed particles within the parametric space will move toward the minimum, that is, the troughs at the bottom of the landscape. The initial positions of the N particles in the swarm are shown in Figure 10(a), where N equals to 10 in this study. The movement of one particle during the PSO iteration is plotted in Figure 10(b).

Figure 11 plots the histogram of the PSO method in terms of run time and number of iteration counts based on the 1000 runs. This figure shows that majority of the 1000 runs have a run time and iteration count around the averaged value of 126 μs and 89.7, respectively. Such small deviations (i.e., smaller standard deviation values) indicate that the performance of the PSO method is rather stable in terms of run time and iteration counts.

During particle evolutions in the PSO method, the norm of the difference between the global best directions $\boldsymbol{q}_{ib}$ and the true minimum of the objective function $\boldsymbol{q}^*$ decreases in a zigzag pattern as plotted in a semi-log plot in Figure 12, characteristics of the PSO convergence.

5.2. *Finite deformation anisotropic damage model*

The second numerical example is the bifurcation analysis of a finite deformation anisotropic damage model subjected to a uniaxial tension test. This material model is developed by Chen *et al*. [37] and is motivated to capture behavior of composite materials containing isotropic elasto-plastic matrix and direction-dependent microfiber components. This is a much more complex material model to evaluate the performance of different numerical bifurcation methods. The model formulation is

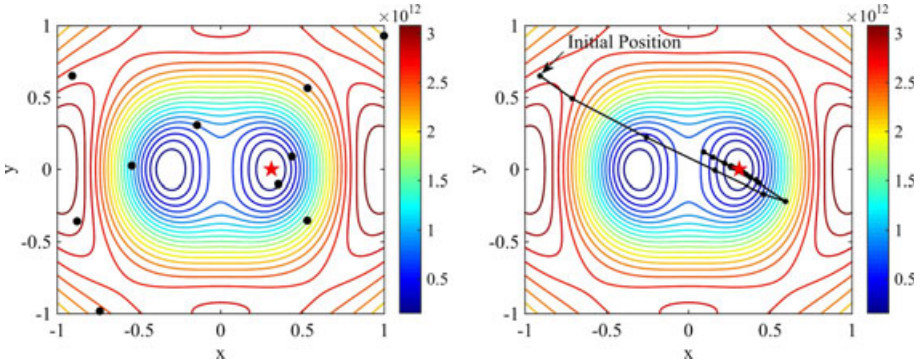

Figure 10. PSO particles movements during the plane strain compression test on the Drucker–Prager model: (a) initial and final converged locations of particles in the swarm (the solid black circles indicate the initial particle positions and the red star is the final converged solution); (b) evolution of one particle position during the PSO iteration (the red star is the final converged location).

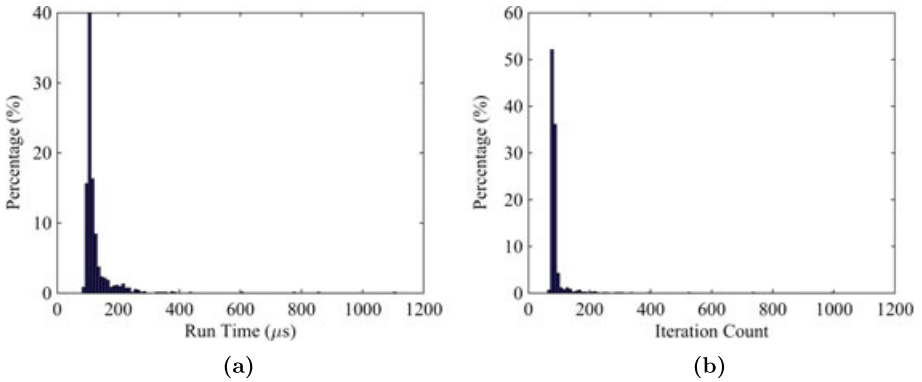

Figure 11. The histogram computed from 1000 runs of (a) run time, and (b) number of iterations, for the bifurcation analysis on the Drucker–Prager model using the PSO method.

DOI: 10.1002/nag

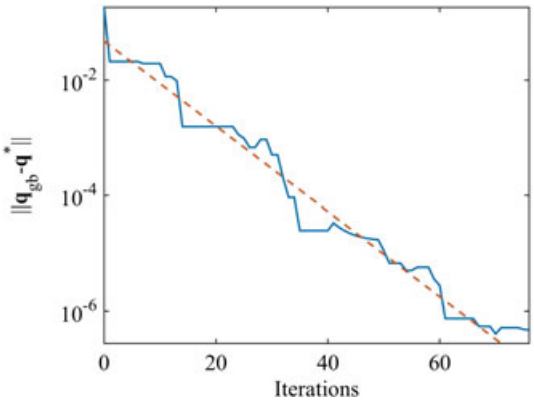

Figure 12. The convergence of the PSO method in the Drucker–Prager example. The red dash line is a linear fitting of the convergence plot on this semi-log scale ($\log_{10}(y) = -0.07381x - 1.321,\ R^2 = 0.9734$).

briefly presented here. Derivation of the tangent modulus is quite involved, and details are included in the Appendix A.

5.2.1. Model formulation. The stress and constitutive tangent of the finite deformation anisotropic damage model are derived from a strain-energy function that has the following form Chen *et al*. [37]

$$\Psi(\boldsymbol{C}, \boldsymbol{M}_i, \xi^{\mathrm{m}}, \xi_i^{\mathrm{f}}) = (1-\xi^{\mathrm{m}}) f^{\mathrm{m}} \Psi^{\mathrm{m}}(\boldsymbol{C}) + \sum_{i=1}^{N} (1-\xi_i^{\mathrm{f}}) f_i^{\mathrm{f}} \Psi_i^{\mathrm{f}}(\boldsymbol{C}, \boldsymbol{M}_i) \tag{24}$$

where $\boldsymbol{C}$ is the right Cauchy–Green tensor; $\boldsymbol{M}_i$ is a unit vector characterizing the preferred fiber direction; f^{m} and f_i^{f} are the volume fraction of the matrix and ith fiber; N is the number of fiber terms; ξ^{m} and ξ_i^{f} are the damage parameter corresponding to the matrix and the ith fibers, respectively. In the following example, we assume that there are two preferred fiber directions, that is, $N = 2$.

Function Ψ^{m} and Ψ_i^{f} are the undamaged energy functions for matrix and ith fiber, respectively. Here, we adopt the following particular forms

$$\Psi^{\mathrm{m}}(\boldsymbol{C}) = U(J) + W(\bar{\boldsymbol{b}}^e) \tag{25}$$

$$\Psi_i^{\mathrm{f}}(\boldsymbol{C}, \boldsymbol{M}_i) = \frac{k_i}{q_i}\{\exp[q_i(I_{4i}-1)^2]\} \tag{26}$$

where k_i and q_i are elastic constants for the ith fiber; I_{4i} is a stress invariant defined as

$$I_{4i} = \boldsymbol{M}_i \cdot (\boldsymbol{C} \cdot \boldsymbol{M}_i) \tag{27}$$

$U(J)$ and $W(\bar{\boldsymbol{b}}^e)$ are the volumetric and deviatoric part of the strain energy given as

$$U(J) = \frac{\kappa}{2}\left(\frac{1}{2}(J^2-1) - \log(J)\right) \tag{28}$$

$$W(\bar{\boldsymbol{b}}^e) = \frac{\mu}{2}(\mathrm{tr}(\bar{\boldsymbol{b}}^e) - 3) \tag{29}$$

where κ and μ are the bulk and shear modulus of the matrix, respectively, J is the determinant of the deformation gradient, and $\bar{\boldsymbol{b}}^e$ is the elastic left Cauchy–Green tensor. The isotropic elasto-plastic matrix component is modeled using a finite deformation J_2-type plasticity model with the yield function F given by

DOI: 10.1002/nag

$$F = ||\text{Dev}(\boldsymbol{S})|| - \sqrt{\frac{2}{3}}[Y_0 + H(\epsilon^p)] \tag{30}$$

where $\boldsymbol{S}$ is the second Piola–Kirchhoff stress tensor, Dev is the deviatoric operator, Y_0 is the initial yield strength, and $H(\epsilon^p)$ is the hardening function of the equivalent plastic strain ϵ^p. A non-linear hardening function is adopted here [52]

$$H(\epsilon^p) = K\epsilon^p + Y_\infty[1 - \exp(-\delta\epsilon^p)] \tag{31}$$

where K is the hardening modulus, Y_∞ is the residual strength, and δ is the saturation exponent.

For the evolution law of the scalar damage parameters ξ^{m} and ξ_i^{f}, we adopt the following exponential form [53]

$$\xi(\alpha) = \xi_\infty[1 - \exp(-\alpha/\tau)] \tag{32}$$

where ξ_∞ is the dimensionless maximum damage and τ is referred to as the damage saturation parameter. Different sets of maximum damage and damage saturation parameters will be used for the matrix and 'microfiber' terms. The parameter α is defined as the maximum thermodynamic force [53]

$$\alpha(t) = \max_{s\in[0,t]} \Psi(s) \tag{33}$$

The fourth-order tangent moduli for second Piola–Kirchhoff stress $\boldsymbol{S}$ and Lagrangian strain $\boldsymbol{E}$ conjugate pair can be computed by taking the second-order derivative with respect to $\boldsymbol{E}$ of the free energy function (24) as

$$\mathbb{A} = (1 - \xi^{\text{m}})\mathbb{A}^{\text{m}} + \sum_i^n (1 - \xi_i^{\text{f}})\mathbb{A}_i^{\text{f}} - \xi^{\text{m}'}(\boldsymbol{S}^{\text{m}} \otimes \boldsymbol{S}^{\text{m}}) - \sum_i^n \xi_i^{\text{f}'}(\boldsymbol{S}_i^{\text{f}} \otimes \boldsymbol{S}_i^{\text{f}}) \tag{34}$$

Table III. Material properties for the finite deformation anisotropic damage model.

Matrix		*Fibers*	
Elastic modulus	$E = 98000$ MPa	Elasticity constants	$k_1 = k_2 = 1000$ MPa
Poissons Ratio	$\nu = 0.37$	Elasticity constants	$q_1 = q_2 = 0.1$
Damage variable	$\xi_\infty^{\text{m}} = 1.0$	Damage variable	$\xi_{\infty(1)}^{\text{f}} = \xi_{\infty(2)}^{\text{f}} = 1.0$
Damage variable	$\tau^{\text{m}} = 40000.0$	Damage variable	$\tau_1^{\text{f}} = \tau_2^{\text{f}} = 400.0$
Volume fraction	$f^{\text{m}} = 0.2$	Volume fraction	$f_1^{\text{f}} = f_2^{\text{f}} = 0.4$
Hardening modulus	$K = 500$ MPa	Direction vector	$\boldsymbol{M}_1 = \{0.5,\ 0.866,\ 0.0\}$
Yield strength	$Y = 1267$ MPa		$\boldsymbol{M}_2 = \{0.5, -0.866,\ 0.0\}$
Saturation exponent	$\delta = 46.0$		
Saturation Modulus	$Y_\infty = 500$ MPa		

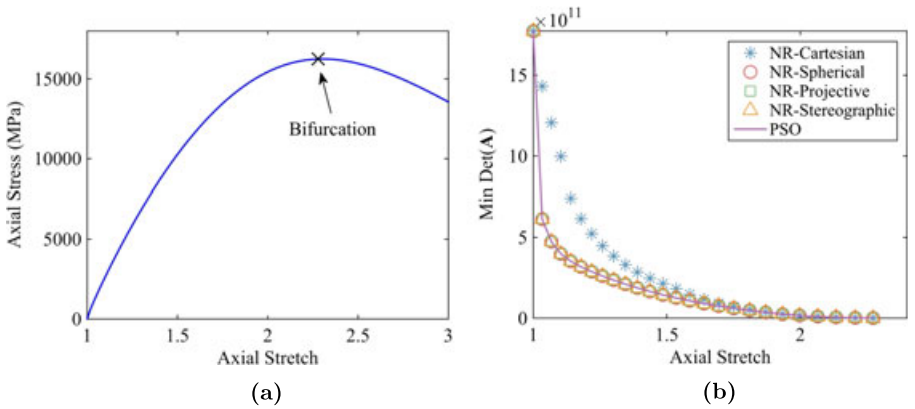

Figure 13. Uniaxial tension test on the finite deformation damage model: (a) axial stress versus axial stretch behavior and (b) degradation of min(det $\boldsymbol{A}$).

DOI: 10.1002/nag

where $\xi^{m'}$ and $\xi^{f'}$ are the derivatives, with respect to α, of the damage parameters defined in (32) for the matrix and the ith fiber, respectively; $\boldsymbol{S}^{m}$ and $\boldsymbol{S}_i^{f}$ are the undamaged second Piola–Kirchhoff stress for the matrix and the ith fiber; $\mathbb{A}^{m}$ and $\mathbb{A}_i^{f}$ are the undamaged tangent moduli tensors. Detailed derivations of these tangents are included in Appendix A.

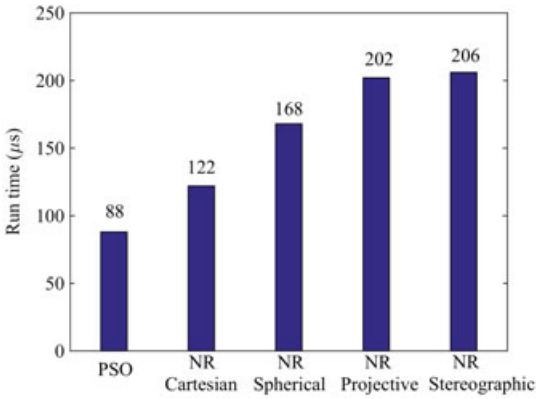

Figure 14. Uniaxial tension test on the finite deformation model: comparison of the run time (in μs) for different numerical approaches.

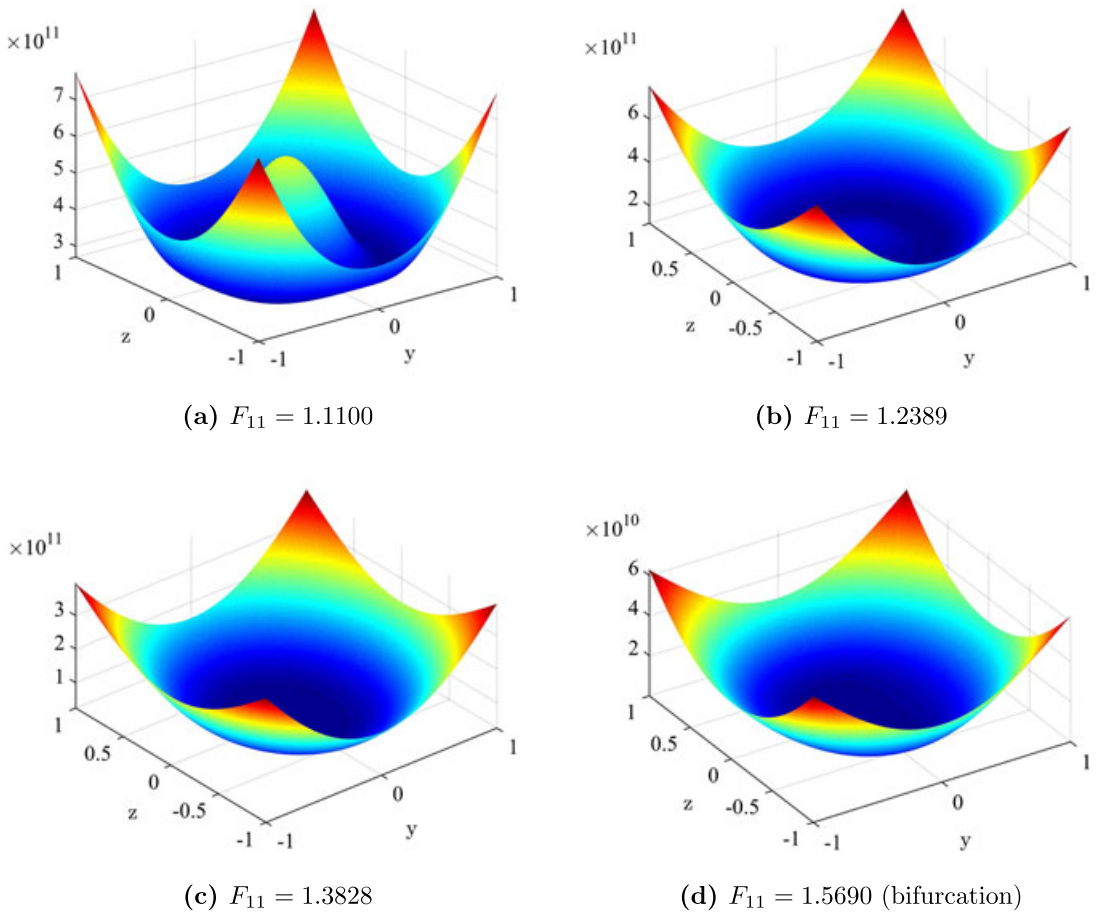

(a) $F_{11} = 1.1100$ (b) $F_{11} = 1.2389$

(c) $F_{11} = 1.3828$ (d) $F_{11} = 1.5690$ (bifurcation)

Figure 15. Cartesian parameterization: landscapes of det A for the uniaxial tension test of the finite deformation cladding-hydride damage model at different axial stretch levels.

DOI: 10.1002/nag

The bifurcation condition (1) at finite strain requires the tangent $\mathbb{C}$ obtained as the second derivative of the strain energy with respect to the deformation gradient $\boldsymbol{F}$. The tangent $\mathbb{A}$ in (34) can be converted to $\mathbb{C}$ using the following relation (in indicial notation) [22]

$$\mathbb{C}_{ijkl} = \tilde{S}_{lj}\delta_{ik} + F_{ip}\mathbb{A}_{pjlq}F_{kq} \tag{35}$$

where $\tilde{S}_{lj}$ is the total effective second Piola–Kirchhoff stress accounting for the damage, that is, $\tilde{\boldsymbol{S}} = (1-\xi^m)\boldsymbol{S}^m + \sum_i^n (1-\xi_i^{\mathrm{f}})\boldsymbol{S}_i^f$.

5.2.2. Uniaxial tension test. The finite deformation anisotropic damage model is subjected to uniaxial tension with material parameters summarized in Table III. The unit vector $\boldsymbol{M}_i$ characterizes the fiber direction.

Figure 13(a) plots the axial stress versus axial stretch (the axial component of the deformation gradient) along with the point material bifurcation is detected. Figure 13(b) shows the degradation of min(det $\boldsymbol{A}$) for all five numerical approaches. As in the previous numerical example, all numerical approaches detect the material bifurcation at the same time, that is, when the axial component of the deformation gradient $F_{11} = 1.5690$ and the corresponding bifurcation direction is given in terms of the unit vector $\boldsymbol{n} = (0.950726,\ 0,\ -0.310032)$.

Comparison of the computational cost of different numerical approaches is plotted in Figure 14. Again, the proposed PSO method is much more efficient in terms of run time. For NR approaches, the Cartesian parameterization requires the least amount of computation time.

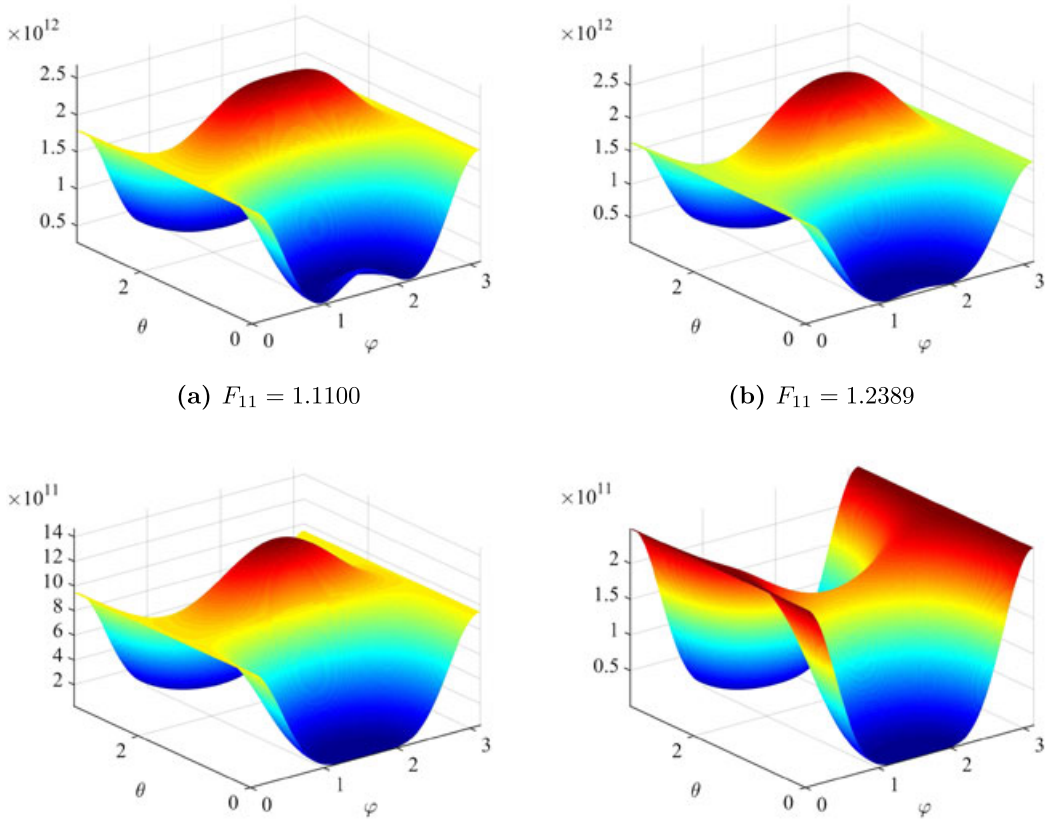

(a) $F_{11} = 1.1100$ (b) $F_{11} = 1.2389$

(c) $F_{11} = 1.3828$ (d) $F_{11} = 1.5690$ (bifurcation)

Figure 16. Spherical parameterization: landscapes of det A for the uniaxial tension test of the finite deformation cladding-hydride damage model at different axial stretch levels.

DOI: 10.1002/nag

To gain insights into the complexity and evolution of the determinant function, we plot landscapes of determinant functions at different loading stages in Figures 15 to 17. It can be seen that landscapes of the determinant functions evolve and exhibit great changes as loading progresses. The only exception is the Cartesian parameterization, which remains approximately bowl-like shape. As pointed out by Mota *et al*. [22], this unique characteristic makes the Cartesian parameterization more robust for NR-based numerical approach.

Similar to the DP model example, a robustness study is performed by randomly selecting initial guess for NR-based approaches. Using the material tangent at the onset of bifurcation, 1000 repeated runs of numerical bifurcation analysis are performed. The results are visualized in Figure 18.

Also, Table IV summarizes and compares the computation time and the success rate of the PSO algorithm and the NR-based approaches. As in the DP model example, the NR-based approaches all start with an initial sweep of N number of randomly placed points within the parametric space. Again, the proposed PSO method is able to correctly detect material bifurcation 100% of the 1000 runs with an averaged run time of just 88.4μs. Recall the results of success rate, averaged run time and iteration count presented in Table II of the DP model example, we found the proposed PSO method is consistently stable in terms of both computational cost and robustness. The proposed PSO method demonstrates superior performance compared with conventional NR-based method for material bifurcation analysis.

Remark 5

The proposed PSO-based numerical algorithm has been tested in this section on two continuum constitutive models under two loading scenarios. Also, more complex loading paths have been

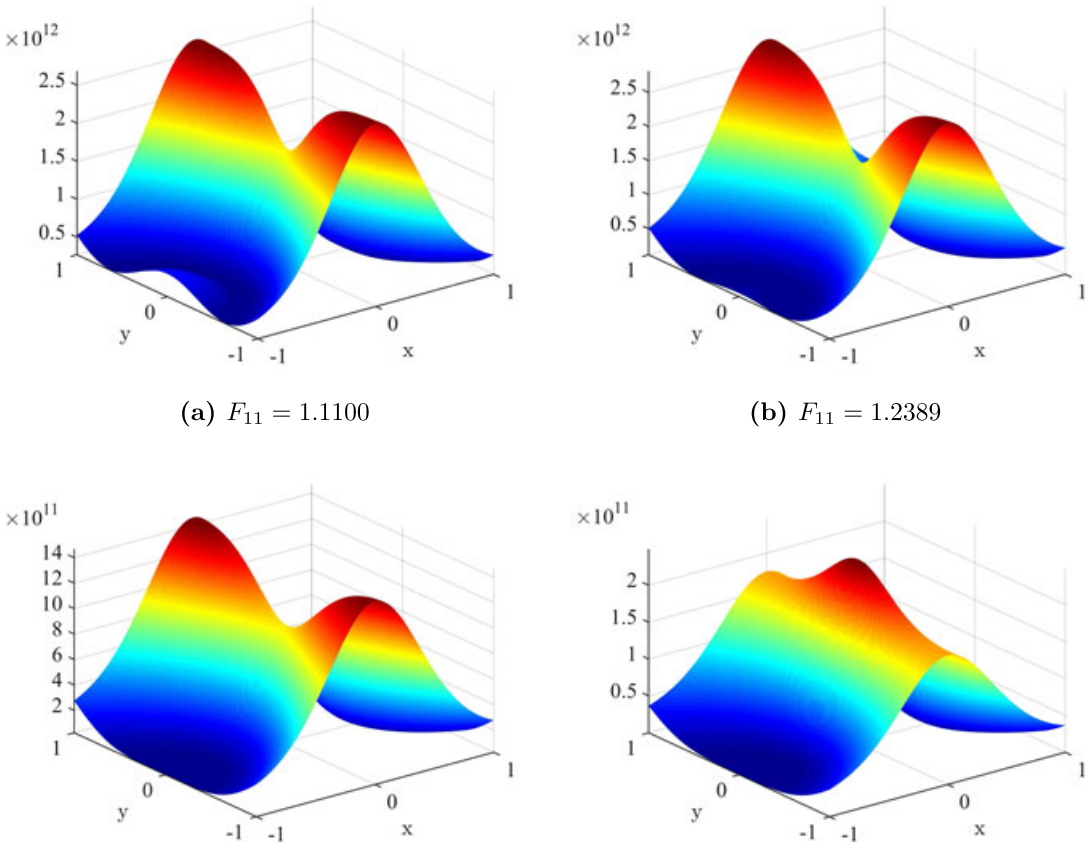

(a) $F_{11} = 1.1100$ (b) $F_{11} = 1.2389$

(c) $F_{11} = 1.3828$ (d) $F_{11} = 1.5690$ (bifurcation)

Figure 17. Stereographic parameterization: landscapes of det A for the uniaxial tension test of the finite deformation cladding-hydride damage model at different axial stretch levels.

DOI: 10.1002/nag

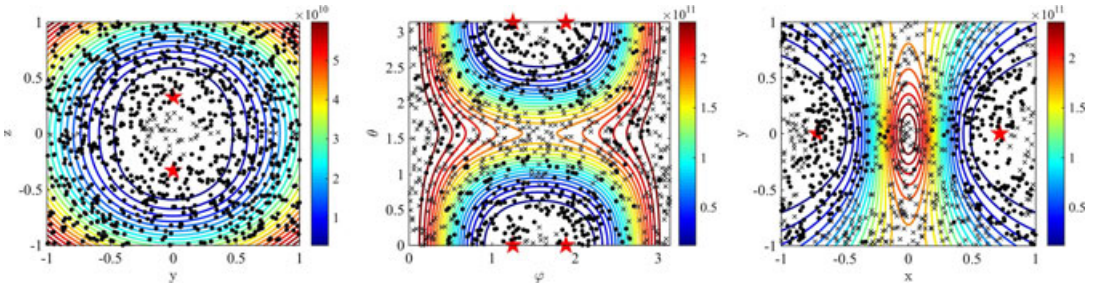

(a) Cartesian (b) Spherical (c) Stereographic

Figure 18. Robustness study for NR-based approach with a single random initial guess for minimizing the determinant function at bifurcation of finite deformation damage model.

Table IV. Success rate and averaged computation time of different numerical approaches with random initial points (for NR-based approaches) or random initial particle positions (for the PSO algorithm).

	PSO	NR-Cartesian	NR-Spherical	NR-Projective	NR-Stereographic
Success rate (%)	100	75.8	84.9	81.9	63.6
Iteration count	66.2	7.06	6.60	8.77	6.46
Run time (μs)	88.4	283	362	516	326

The averaged iteration count and run time are computed using successful runs only.

simulated using the material models presented, where the PSO algorithm shows consistent and robust performance. Because the PSO algorithm is able to handle optimization of very complex objective functions, it could potentially be applied to even more complex material models, for example, materials with extreme incremental nonlinearity [54, 55], which will be looked into in future investigations.

6. CONCLUSIONS

In this work, we propose a novel numerical method to the solutions of material bifurcation problem in small and finite deformation computational inelasticity. The method is based on an intelligence optimizer called the PSO, which is used to solve the constrained minimization problem of finding the minimum of the determinant of the acoustic tensor and the associated bifurcation directions. The performance of the proposed PSO method is tested through numerical bifurcation analysis on both small and finite deformation material models with increasing complexity. Common NR-based numerical approaches are also implemented to compare with the proposed PSO method. In summary, we find that

1. The proposed approach is simple in formulation and convenient for implementation. This is in contrast to conventional NR-based approaches, which require derivation and evaluation of gradient of the complex determinant function.
2. A small deformation plasticity model for frictional-dilative geomaterial and a finite deformation anisotropic damage model under simple loading provides sufficiently complexity to evaluate the proposed numerical approach to detect material bifurcation.
3. For the conventional NR-based approaches, the efficiency and robustness are greatly affected by the quality of initial guess from sampling stage. Among four parameterizations investigated, the Cartesian parametrization is the most robust and provides the best balance between computational efficiency and robustness.
4. The proposed PSO-based approach shows consistently superior performance in terms of both computational efficiency and robustness when applied to small and finite deformation material models with increasing complexity. The proposed approach provides a valuable tool for efficient and robust numerical analysis of material bifurcation in computational inelasticity.

DOI: 10.1002/nag

APPENDIX A: DERIVATION OF TANGENT MODULI FOR THE FINITE DEFORMATION ANISOTROPIC DAMAGE MODEL

In this section, details of the derivation to obtain the undamaged tangent moduli of the matrix $\mathbb{A}^m$ and fibers $\mathbb{A}_i^f$ in (34) are presented. Notations and symbols used in the derivation are as follows: the symbol '$\cdot$' denotes an inner product of two vectors (e.g., $\boldsymbol{a}\cdot\boldsymbol{b} = a_i b_i$), or a single contraction of adjacent indices of two tensors (e.g., $\boldsymbol{c}\cdot\boldsymbol{d} = c_{ij}d_{jk}$); the symbol ':' denotes an inner product of two second-order tensors (e.g., $\boldsymbol{c} : \boldsymbol{d} = c_{ij}d_{ij}$), or a double contraction of adjacent indices of tensors of rank two and higher (e.g., $\mathbb{C} : \boldsymbol{\epsilon} = C_{ijkl}\epsilon_{kl}$); the symbol '$\otimes$' denotes a juxtaposition, that is, $(\boldsymbol{a}\otimes\boldsymbol{b})_{ij} = a_i b_j$.

A.1 Tangent modulus of the isotropic elastoplastic matrix

For the tangent modulus of the isotropic elastoplastic matrix, denoted as $\mathbb{A}^m$ in (34), an elastic tangent $\mathbb{A}^{me}$ will be returned if the material undergoes elastic deformation and an elstoplastic tangent $\mathbb{A}^{mep}$ will be returned for plastic deformation.

In the elastic domain, the volumetric part of the undamaged second Piola–Kirchhoff stress tensor $\boldsymbol{S}^{mV}$ and the elastic tangent moduli $\mathbb{A}^{mV}$ are calculated by taking the first and second derivative of the volumetric strain energy $U(J)$ defined in (25) with respect to the Lagrangian strain $\boldsymbol{E}$. Note that $\boldsymbol{E} = \frac{1}{2}(\boldsymbol{C} - \boldsymbol{I})$, the derivative yields

$$\boldsymbol{S}^{mV} = f^m U' J \boldsymbol{C}^{-1} \tag{A.1}$$

$$\mathbb{A}^{mV} = f^m[U'' J^2 \boldsymbol{C}^{-1}\otimes\boldsymbol{C}^{-1} + U' J \boldsymbol{C}^{-1}\otimes\boldsymbol{C}^{-1} - U' J(\boldsymbol{C}_{ik}^{-1}\otimes\boldsymbol{C}_{jl}^{-1} + \boldsymbol{C}_{il}^{-1}\otimes\boldsymbol{C}_{jk}^{-1})] \tag{A.2}$$

where $\boldsymbol{C}$ is the right Cauchy–Green tensor, J is the determinant of the deformation gradient $\boldsymbol{F}$, U' is the derivative of volumetric strain energy U with respect to $\boldsymbol{E}$.

Similarly, the deviatoric part of second Piola–Kirchhoff stress tensor $\boldsymbol{S}^{mDev}$ or $\mathrm{Dev}(\boldsymbol{S}^{\boldsymbol{m}})$ and the elastic tangent moduli $\mathbb{A}^{mDev}$ can be calculated as

$$\boldsymbol{S}^{mDev} = f^m \mu J^{-2/3} \boldsymbol{C}^{p-1} : \mathbb{P}^{Dev} \tag{A.3}$$

$$\begin{aligned}\mathbb{A}^{mDev} = f^m \Bigg[&\frac{1}{3}\mu J^{-2/3}(\boldsymbol{C}^{p-1} : \boldsymbol{C})(\boldsymbol{C}_{ik}^{-1}\otimes\boldsymbol{C}_{jl}^{-1} + \boldsymbol{C}_{il}^{-1}\otimes\boldsymbol{C}_{jk}^{-1})\\ &-\frac{2}{3}\mu J^{-2/3}\boldsymbol{C}^{p-1} : \mathbb{P}^{Dev}\otimes\boldsymbol{C}^{-1} - \frac{2}{3}\mu J^{-2/3}\boldsymbol{C}^{-1}\otimes\boldsymbol{C}^{p-1}\Bigg]\end{aligned} \tag{A.4}$$

where $\mathbb{P}^{Dev} = \mathbb{I} - \frac{1}{3}\boldsymbol{C}\otimes\boldsymbol{C}^{-1}$ is the fourth-order deviatoric operator tensor defined in the reference configuration; $\mathbb{I}$ is the fourth-order identity tensor.

Thus, the undamaged second Piola–Kirchhoff stress and the elastic tangent modulus of the matrix in elastic domain can be written as

$$\boldsymbol{S}^m = f^m \frac{\partial \boldsymbol{\Psi}^m}{\partial \boldsymbol{E}} = \boldsymbol{S}^{mV} + \boldsymbol{S}^{mDev} \tag{A.5}$$

$$\mathbb{A}^{me} = \frac{\partial \boldsymbol{S}^m}{\partial \boldsymbol{E}} = \mathbb{A}^{mV} + \mathbb{A}^{mDev} \tag{A.6}$$

In the plastic domain, the elasto-plastic tangent modulus can be derived using consistent condition, yield function and flow rule, and is given as [56]

$$\mathbb{A}^{mep} = \mathbb{A}^{me} - \frac{\frac{\partial F}{\partial \boldsymbol{E}}\otimes\frac{\partial F}{\partial \boldsymbol{E}}}{\frac{\partial F}{\partial \boldsymbol{E}^p} : \mathbb{M}^{-1} : \frac{\partial F}{\partial \boldsymbol{E}} - \frac{\partial F}{\partial Q}\cdot\dot{Q}} \tag{A.7}$$

DOI: 10.1002/nag

where F is the yield function, $\boldsymbol{E}^p$ is the Lagrangian plastic strain, Q is the internal variable, $\mathbb{M}$ is the plastic dissipation tangent moduli, defined as [56]

$$\mathbb{M} = \frac{\partial^2 \boldsymbol{\Psi}^m}{\partial \boldsymbol{E} \partial \boldsymbol{E}^{\boldsymbol{p}}} \tag{A.8}$$

The yield function is defined in (30) and repeated here

$$F = ||\mathrm{Dev}(\boldsymbol{S})|| - \sqrt{\frac{2}{3}}[Y_0 + H(\epsilon^p)] \tag{A.9}$$

In the yield function (A.9), the norm of the deviatoric second Piola–Kirchhoff stress tensor $||\mathrm{Dev}(\boldsymbol{S})||$ in the reference configuration is defined as [56]

$$||\mathrm{Dev}(\boldsymbol{S})|| = \sqrt{[\mathrm{Dev}(\boldsymbol{S})\boldsymbol{C}] : [\mathrm{Dev}(\boldsymbol{S})\boldsymbol{C}]^T} \tag{A.10}$$

where the right Cauchy–Green tensor $\boldsymbol{C}$ plays the role of a metric tensor [56]. By using the chain rule

$$\frac{\partial ||\mathrm{Dev}(\boldsymbol{S})||}{\boldsymbol{C}} = \frac{[\mathrm{Dev}(\boldsymbol{S})\boldsymbol{C}]^T}{||\mathrm{Dev}(\boldsymbol{S})||} : \frac{\partial \mathrm{Dev}(\boldsymbol{S})\boldsymbol{C}}{\partial \boldsymbol{C}} \tag{A.11}$$

Denote first term on the left-hand side as

$$\boldsymbol{N} = \frac{[\mathrm{Dev}(\boldsymbol{S})\boldsymbol{C}]^T}{||\mathrm{Dev}(\boldsymbol{S})||} \tag{A.12}$$

The second term on the left-hand side of (A.11) can be calculated as (in indicial notation)

$$\begin{aligned} \frac{\partial \mathrm{Dev}(\boldsymbol{S}_{im})\boldsymbol{C}_{mj}}{\partial \boldsymbol{C}_{kl}} &= \frac{\partial \mathrm{Dev}(\boldsymbol{S}_{im})}{\partial \boldsymbol{C}_{kl}}\boldsymbol{C}_{mj} + \mathrm{Dev}(\boldsymbol{S}_{im})\frac{\partial \boldsymbol{C}_{mj}}{\partial \boldsymbol{C}_{kl}} \\ &= \frac{1}{2}\mathbb{A}^{Dev}_{imkl}\boldsymbol{C}_{mj} + \mathrm{Dev}(\boldsymbol{S}_{im})\mathbb{I}_{mjkl} \end{aligned} \tag{A.13}$$

where $\mathbb{I}$ is the fourth-order identity tensor. Combing (A.12) and (A.13) yields the derivative of yield function F with respect to the Lagrangian strain $\boldsymbol{E}$ as

$$\frac{\partial F}{\partial \boldsymbol{E}_{kl}} = 2\frac{\partial ||\mathrm{Dev}(\boldsymbol{S})||}{\partial \boldsymbol{C}_{kl}} = \boldsymbol{N}_{ij} : (\mathbb{A}^{Dev}_{imkl}\boldsymbol{C}_{mj} + 2\mathrm{Dev}(\boldsymbol{S}_{im})\mathbb{I}_{mjkl}) \tag{A.14}$$

The plastic dissipation tangent can be calculated as

$$\mathbb{M}_{ijkl} = \frac{\partial \boldsymbol{S}_{ij}}{\partial \boldsymbol{E}^p_{kl}} = -\mu J^{-2/3}(\boldsymbol{C}^{p-1}_{mk} \otimes \boldsymbol{C}^{p-1}_{nl} + \boldsymbol{C}^{p-1}_{ml} \otimes \boldsymbol{C}^{p-1}_{nk}) : \mathbb{P}^{Dev}_{mnij} \tag{A.15}$$

Recalling that

$$\frac{\partial \mathrm{Dev}(\boldsymbol{S}_{im})\boldsymbol{C}_{mj}}{\partial \boldsymbol{E}^p_{kl}} = \frac{\partial \boldsymbol{S}_{im}}{\partial \boldsymbol{E}^p_{kl}}\boldsymbol{C}_{mj} = \mathbb{M}_{imkl}\boldsymbol{C}_{mj} \tag{A.16}$$

By chain rule and using (A.16), the following terms in (A.7) can be obtained

$$\frac{\partial F}{\boldsymbol{E}^p_{kl}} = \frac{(\mathrm{Dev}(\boldsymbol{S})\boldsymbol{C})^T}{||\mathrm{Dev}(\boldsymbol{S})||} : \frac{\partial \mathrm{Dev}(\boldsymbol{S})\boldsymbol{C}}{\partial \boldsymbol{E}^p} = \boldsymbol{N}_{ij} : (\mathbb{M}_{imkl}\boldsymbol{C}_{mj}) \tag{A.17}$$

$$\frac{\partial F}{\partial \boldsymbol{E}^p_{kl}} : \mathbb{M}^{-1}_{klpq} = \boldsymbol{N}_{ij} : (\mathbb{M}_{imkl}\boldsymbol{C}_{mj}) : \mathbb{M}^{-1}_{klpq} = \boldsymbol{N}_{pm}\boldsymbol{C}_{mq} \tag{A.18}$$

DOI: 10.1002/nag

For the hardening terms involving internal variable Q, which is the equivalent plastic strain ϵ^p in this model, the following gradient can be easily derived

$$\frac{\partial F}{\partial Q} = \frac{\partial F}{\partial \epsilon^p} = -\sqrt{\frac{2}{3}}[K + Y_\infty \delta \exp(-\delta \epsilon^p)] \tag{A.19}$$

$$\dot{Q} := \frac{\partial \epsilon^p}{\partial \gamma} = \sqrt{\frac{2}{3}} \tag{A.20}$$

where K is the hardening modulus, Y_∞ is the residual strength, δ is the saturation exponent, γ is the cumulative plastic strain.

A.2 Tangent modulus of the direction-dependent fibers

Taking the derivative of the strain energy Ψ_i^f of the fibers defined in (26) with respect to the Lagrangian strain $\boldsymbol{E}$ yields the undamaged stress $\boldsymbol{S}_i^f$, which can be written as

$$\boldsymbol{S}_i^f = {f_i}^f \frac{\partial \Psi_i^f}{\partial \boldsymbol{E}} = 2{f_i}^f \frac{\partial \Psi_i^f}{\partial \boldsymbol{C}} = 2{f_i}^f k_i (I_{4i} - 1) \exp[q_i (I_{4i} - 1)^2] \boldsymbol{M}_i \otimes \boldsymbol{M}_i \tag{A.21}$$

where f_i^{f} is the volume fraction of the ith fiber, k_i and q_i are elastic constants, I_{4i} is a stress invariant defined in (27), $\boldsymbol{M}_i$ is a unit vector characterizing the preferred fiber direction.

The undamaged tangent modulus can be calculated as

$$\mathbb{A}_i^f = 2\frac{\partial \boldsymbol{S}_i^f}{\partial \boldsymbol{C}} = 8.0{f_i}^f k_i [1.0 + 2.0 q_i (I_{4i} - 1)^2] \exp[q_i (I_{4i} - 1)^2] \boldsymbol{M}_i \otimes \boldsymbol{M}_i \tag{A.22}$$

ACKNOWLEDGEMENTS

The second author wishes to acknowledge the support of the NASA South Carolina Space Grant Consortium REAP Award (2020814) under the contract number 521179-RP-CMChen. The authors wish to thank the editor and the anonymous reviewers for their constructive comments that helped improve this paper.

REFERENCES

1. Borja RI. Conditions for instabilities in collapsible solids including volume implosion and compaction banding. *Acta Geotechnica* 2006; **1**(2):107–122.
2. Borja RI. Condition for liquefaction instability in fluid-saturated granular soils. *Acta Geotechnica* 2006; **1**(4): 211–224.
3. Sun WC. A unified method to predict diffuse and localized instabilities in sands. *Geomechanics and Geoengineering* 2013; **8**(2):65–75.
4. Neilsen MK, Schreyer HL. Bifurcations in elastic-plastic materials. *International Journal of Solids and Structures* 1993; **30**(4):521–544.
5. Hill R. A general theory of uniqueness and stability in elastic-plastic solids. *Journal of the Mechanics and Physics of Solids* 1958; **6**(3):236–249.
6. Valanis KC. Banding and stability in plastic materials. *Acta Mechanica* 1989; **79**(1-2):113–141.
7. Bigoni D, Hueckel T. Uniqueness and localization–I. Associative and non-associative elastoplasticity. *International Journal of Solids and Structures* 1991; **28**(2):197–213.
8. Rudnicki JW, Rice JR. Conditions for the localization of deformation in pressure-sensitive dilatant materials. *Journal of the Mechanics and Physics of Solids* 1975; **23**(6):371–394.
9. Rice JR. The localization of plastic deformation. *In Theoretical and Applied Mechanics (Proceedings of the 14th International Congress on Theoretical and Applied Mechanics, Delft, 1976, ed. W.T. Koiter)*, Vol. 1, North-Holland Publishing Co.: Amsterdam, Netherlands, 1976; 207–220.
10. Leroy Y, Nacar A, Needleman A, Ortiz M. A finite element method for localization analysis. *Advances in Inelastic Analysis, ASME, AMD* 1987; **88**:97–106.
11. Runesson K, Ottosen NS, Dunja P. Discontinuous bifurcations of elastic-plastic solutions at plane stress and plane strain. *International Journal of Plasticity* 1991; **7**(1):99–121.

DOI: 10.1002/nag

12. Ottosen NS, Runesson K. Properties of discontinuous bifurcation solutions in elasto-plasticity. *International Journal of Solids and Structures* 1991; **27**(4):401–421.
13. Schröder DIJ, Miehe C. Post-critical discontinuous localization analysis of small-strain softening elastoplastic solids. *Archive of Applied Mechanics* 1994; **64**(4):267–285.
14. Steinmann P, Miehe C, Stein E. On the localization analysis of orthotropic hill type elastoplastic solids. *Journal of the Mechanics and Physics of Solids* 1994; **42**(12):1969–1994.
15. Steinmann P, Stein E. On the numerical treatment and analysis of finite deformation ductile single crystal plasticity. *Computer Methods in Applied Mechanics and Engineering* 1996; **129**(3):235–254.
16. Cervera M, Chiumenti M, Di Capua D. Benchmarking on bifurcation and localization in J_2 plasticity for plane stress and plane strain conditions. *Computer Methods in Applied Mechanics and Engineering* 2012; **241**:206–224.
17. Ortiz M, Leroy Y, Needleman A. A finite-element method for localized failure analysis. *Computer Methods in Applied Mechanics and Engineering* 1987; **61**(2):189–214.
18. Sanborn SE, Prévost JH. Frictional slip plane growth by localization detection and the extended finite element method (XFEM). *International Journal for Numerical and Analytical Methods in Geomechanics* 2011; **35**(11):1278–1298.
19. Andrade JE, Borja RI. Capturing strain localization in dense sands with random density. *International Journal for Numerical Methods in Engineering* 2006; **67**(11):1531–1564.
20. Mosler J. Numerical analyses of discontinuous material bifurcation: strong and weak discontinuities. *Computer Methods in Applied Mechanics and Engineering* 2005; **194**(9):979–1000.
21. Regueiro RA, Foster CD. Bifurcation analysis for a rate-sensitive, non-associative, three-invariant, isotropic/kinematic hardening cap plasticity model for geomaterials: Part i. small strain. *International Journal for Numerical and Analytical Methods in Geomechanics* 2011; **35**(2):201–225.
22. Mota A, Chen Q, Foulk JW, Ostien JT, Lai Z. A cartesian parametrization for the numerical analysis of material instability. *International Journal for Numerical Methods in Engineering* 2016; **108**(2):156–180.
23. Oliver J, Huespe AE, Cante JC, Diaz G. On the numerical resolution of the discontinuous material bifurcation problem. *International Journal for Numerical Methods in Engineering* 2010; **83**(6):786–804.
24. Eberhart RC, Kennedy J. A new optimizer using particle swarm theory. *Proceedings of the Sixth International Symposium on Micro Machine and Human Science*, Vol. 1, IEEE: New Jersey, US, 1995; 39–43.
25. Eberhart R, Simpson P, Dobbins R. *Computational Intelligence PC Tools*. Academic Press Professional, Inc.: San Diego, CA, USA, 1996.
26. Van den Bergh F, Engelbrecht AP. A convergence proof for the particle swarm optimiser. *Fundamenta Informaticae* 2010; **105**(4):341–374.
27. Poli R, Kennedy J, Blackwell T. Particle swarm optimization. *Swarm Intelligence* 2007; **1**(1):33–57.
28. Feng XT, Chen BR, Yang C, Zhou H, Ding X. Identification of visco-elastic models for rocks using genetic programming coupled with the modified particle swarm optimization algorithm. *International Journal of Rock Mechanics and Mining Sciences* 2006; **43**(5):789–801.
29. Kennedy J. Particle swarm optimization. In *Encyclopedia of Machine Learning*. Springer: New York, USA, 2010; 760–766.
30. Campana EF, Fasano G, Peri D, Pinto A. Particle swarm optimization: Efficient globally convergent modifications. *Proceedings of the III European Conference on Computational Mechanics, Solids, Structures and Coupled Problems in Engineering*, 2006; 412–412.
31. Parsopoulos KE, Vrahatis MN. On the computation of all global minimizers through particle swarm optimization. *IEEE Transactions on Evolutionary Computation* 2004; **8**(3):211–224.
32. Jiang M, Luo YP, Yang SY. Stochastic convergence analysis and parameter selection of the standard particle swarm optimization algorithm. *Information Processing Letters* 2007; **102**(1):8–16.
33. Clerc M, Kennedy J. The particle swarm-explosion, stability, and convergence in a multidimensional complex space. *IEEE Transactions on Evolutionary Computation* 2002; **6**(1):58–73.
34. Salinger AG, Bartett RA, Chen Q, Gao X, Hansen G, Kalashnikova I, Mota A, Muller RP, Nielsen E, Ostien J. *et al* Albany: A component-based partial differential equation code built on trilinos. *Technical Report*, Sandia National Laboratories Livermore: CA; Sandia National Laboratories (SNL-NM): Albuquerque, NM, USA, 2013.
35. Salinger AG, Bartlett RA, Bradley AM, Chen Q, Demeshko IP, Gao X, Hanson GA, Mota A, Muller RP, Nielsen E, Ostien JT, Pawlowski RP, Perego M, Phipps ET, Sun W, Tezaur IK. Albany: Using component-based design to develop a flexible, generic multiphysics analysis code. *International Journal for Multiscale Computational Engineering*. DOI:10.1615/IntJMultCompEng.2016017040.
36. Salinger AG et al. *Albany website*, 2016. https://software.sandia.gov/a lbany. Accessed on 20 June 2016.
37. Chen Q, Ostien JT, Hansen G. Development of a used fuel cladding damage model incorporating circumferential and radial hydride responses. *Journal of Nuclear Materials* 2014; **447**(1):292–303.
38. Hansen GA, Ostien JT, Chen Q. *NEAMS VLTS* project: level 2 milestone summary. *Technical Report SAND2012-5808*, Sandia National Laboratories (SNL-NM): Albuquerque, NM, USA, 2012.
39. Sun WC, Chen Q, Ostien JT. Modeling the hydro-mechanical responses of strip and circular punch loadings on water-saturated collapsible geomaterials. *Acta Geotechnica* 2014; **9**(5):903–934.
40. Chen Q, Ostien JT, Hansen G. Automatic differentiation for numerically exact computation of tangent operators in small- and large-deformation computational inelasticity. *Proceedings of the 143th TMS Annual Meeting & Exhibition*, John Wiley & Sons: Hoboken, New Jersey, USA, 2014; 289.

DOI: 10.1002/nag

41. Pawlowski RP, Phipps ET, Salinger AG. Automating embedded analysis capabilities and managing software complexity in multiphysics simulation, Part I: Template-based generic programming. *Scientific Programming* 2012; **20**(2):197–219.
42. Pawlowski RP, Phipps ET, Salinger AG, Owen SJ, Siefert CM, Staten ML. Automating embedded analysis capabilities and managing software complexity in multiphysics simulation, Part II: Application to partial differential equations. *Scientific Programming* 2012; **20**(3):327–345.
43. Schutte JF, Reinbolt JA, Fregly BJ, Haftka RT, George AD. Parallel global optimization with the particle swarm algorithm. *International Journal for Numerical Methods in Engineering* 2004; **61**(13):2296–2315.
44. Parsopoulos KE, Vrahatis MN. Recent approaches to global optimization problems through particle swarm optimization. *Natural Computing* 2002; **1**(2-3):235–306.
45. Shi Y, Eberhart RC. Parameter selection in particle swarm optimization. In *Evolutionary programming VII*. Springer: Berlin, Germany, 1998; 591–600.
46. Trelea IC. The particle swarm optimization algorithm: convergence analysis and parameter selection. *Information Processing Letters* 2003; **85**(6):317–325.
47. Riget J, Vesterstrøm JS. A diversity-guided particle swarm optimizer-the ARPSO. *Technical Report 2*, Dept. Comput. Sci., Univ. of Aarhus, Aarhus, Denmark, 2002.
48. Blackwell TM. Particle swarms and population diversity. *Soft Computing* 2005; **9**(11):793–802.
49. Drucker DC, Prager W. Soil mechanics and plastic analysis or limit design. *Quarterly of Applied Mathematics* 1952; **10**:157–165.
50. Tu X, Andrade JE, Chen Q. Return mapping for nonsmooth and multiscale elastoplasticity. *Computer Methods in Applied Mechanics and Engineering* 2009; **198**(30):2286–2296.
51. Semnani SJ, White JA, Borja RI. Thermoplasticity and strain localization in transversely isotropic materials based on anisotropic critical state plasticity. *International Journal for Numerical and Analytical Methods in Geomechanics* 2016; **40**(18):2423–2449.
52. Simo JC, Hughes TJR. *Computational Inelasticity*. Springer: New York, 1998.
53. Holzapfel GA. *Nonlinear Solid Mechanics*, Vol. 24. Wiley Chichester: Chichester, UK, 2000.
54. Tjioe M, Borja RI. On the pore-scale mechanisms leading to brittle and ductile deformation behavior of crystalline rocks. *International Journal for Numerical and Analytical Methods in Geomechanics* 2015; **39**(11):1165–1187.
55. Tjioe M, Borja RI. Pore-scale modeling of deformation and shear band bifurcation in porous crystalline rocks. *International Journal for Numerical Methods in Engineering* 2016; **108**(3):183–212.
56. Simo JC. A framework for finite strain elastoplasticity based on maximum plastic dissipation and the multiplicative decomposition: Part I. Continuum formulation. *Computer Methods in Applied Mechanics and Engineering* 1988; **66**(2):199–219.

DOI: 10.1002/nag